J. Mech. Phys. Solids 200 (2025) 106078

Contents lists available at ScienceDirect

Journal of the Mechanics and Physics of Solids

journal homepage: www.elsevier.com/locate/jmps

Thermo-chemo-mechanical model and variational multiscale framework for material and geometric evolution in frontal polymerization

Ignasius P.A. Wijaya [a], Philippe Geubelle [b], Arif Masud [c,*]

[a] Department of Civil and Environmental Engineering, Grainger College of Engineering, University of Illinois Urbana–Champaign, IL 61801, USA
[b] Department of Aerospace Engineering, Grainger College of Engineering, University of Illinois Urbana–Champaign, IL 61801, USA
[c] Department of Civil and Environmental Engineering, Department of Mechanical Science and Engineering, Grainger College of Engineering, University of Illinois Urbana–Champaign, IL 61801, USA

A R T I C L E I N F O

Keywords:
Frontal polymerization
Traveling reaction fronts
Thermo-chemo-mechanical coupling
Thermodynamic
Evolving material properties
Evolving geometry
Finite deformations
Finite element method
Variational multiscale method

A B S T R A C T

This paper presents a thermodynamically consistent model for thermo-chemo-mechanical processes in frontal polymerization (FP). The model consists of cure kinetics, heat transfer, and finite strain kinematics of nonlinear inelastic solid undergoing finite deformation. The constitutive relations are derived by enforcing non-negative entropy production which implies the existence of cure induced inelastic processes during material property evolution. Rapid curing triggered by thermo-chemical processes results in traveling reaction fronts that traverse the domain, and material properties evolve across these fronts on short time scales, accompanied with chemical expansion/contraction of the constituents. Complexity of the process increases with increased rate of chemical reaction, increased rate of mass transport, and large mechanical deformations. Evolving nonlinearities and coupled thermo-chemo-mechanical effects give rise to spatially localized phenomena that exhibit shear bands, steep gradients, and boundary and/or internal layers. The presence of interfacial effects can also trigger jumps in the fields, leading to further classification as mathematically non-smooth mixed-field problems. These modeling issues require mathematical formulations that can handle rapidly evolving material nonlinearity as well as steep traveling gradients. A stabilized finite element method that is based on the Variational Multiscale (VMS) framework is employed. A unique attribute of the VMS framework is the derivation of the residual-based fine-scale models that represent subgrid scale physics. These models enhance the stability of the numerical method as well as the accuracy of the computed physics. Several test cases are presented that investigate the mathematical attributes of the constitutive model for FP, and the role of enhanced stability and higher spatial accuracy of the proposed stabilized method in free-form printing with evolving polymerization front.

1. Introduction

Frontal polymerization (FP) is a process in which a self-propagating reaction front traverses through the material, converting monomers into polymers (Chechilo et al., 1972; Pojman, 2012; Suslick et al., 2023). A key features of FP is the exothermic reactions that release heat as polymerization progresses, and this local heat generation advances the reaction front in a self-consistent fashion. FP is not only energy-efficient and scalable (Robertson et al., 2018; Ivanoff et al., 2020), it also enables extrusion-based direct ink

* Corresponding author.
E-mail addresses: iwijaya2@illinois.edu (I.P.A. Wijaya), geubelle@illinois.edu (P. Geubelle), amasud@illinois.edu (A. Masud).

https://doi.org/10.1016/j.jmps.2025.106078
Received 18 August 2024; Received in revised form 26 December 2024; Accepted 12 February 2025
Available online 3 March 2025

writing (DIW) with polymers (Aw, 2019; Aw et al., 2022) to manufacture freestanding thermoset structures. Furthermore, FP can be used to fabricate molecularly architected polymers (Paul et al., 2024) and complex patterns in the macrostructure (Lloyd et al., 2021).

Frontal polymerization offers unique opportunities for designing novel materials. However, precise optimization of the processing parameters that control the reaction front encounters certain bottlenecks that pose a challenge to this technology (Suslick et al., 2023; Mariani and Malucelli, 2023). Any variability in material composition can lead to non-uniform polymerization which can in turn affect the quality of the final product. In addition, parameters that control the chemical and physical mechanisms in the processing of FP also need to be optimized to achieve the desired material properties for intended applications (Vyas et al., 2024). Since polymerization reaction is sensitive to the temperature field, carefully managing temperature evolution is critical for controlling the rate of reaction and therefore the speed of propagation of the reaction front. In order to address these technical issues, advanced modeling techniques that can help develop deeper understanding of the thermodynamics of FP are needed. These mathematical models can provide insights into the combined chemical and physical processes that can then be controlled to achieve uniform and self-sustained reaction fronts.

Most FP models presented in the literature are focused on thermo–chemical processes to estimate key characteristics such as maximum temperature and velocity of the moving reaction front (Frulloni et al., 2005; Goli et al., 2018; Kumar et al., 2021; Liu et al., 2024), and stability of the propagating front (Solovyov et al., 1997; Goli et al., 2020). A coupled thermo–chemo–mechanical model for FP is proposed in Kumar et al. (2022) where the monomers and polymers are modeled as elastic solids with evolving material parameters. It is shown that the phase transformation via polymerization can freeze the material in its deformed configuration. This behavior was modeled via an internal variable representing eigenstrains associated with material evolution. The model was then extending to viscoelastic solids for the simulation of FP-DIW to estimate the effect of printing parameters on the deformation of the printed parts (Kumar et al., 2024). Another approach to model the material as viscoelastic fluid where the cured structure is assumed to be rigid is presented in Zakoworotny et al. (2024).

Motivated by the seminal works in Truesdell (1984) and Truesdell and Noll (2004), development of thermodynamically consistent formulations for nonlinear multi-field problems has been pursued by many researchers. Significant contributions have been made in the past decade to the development of fully coupled, continuum models for thermo–chemo–mechanical phenomena. The work of Kannan and Rajagopal (2011) provides a rigorous and detailed presentation on the thermodynamics of chemical reactions in multi-constituent systems. FP in additive manufacturing involves continuous influx of mass that undergoes phase change and material property evolution. As such, the constitutive models need to be developed in the context of open system thermodynamic frameworks. A good discussion on the mathematical complexities that arise when dealing with open system thermodynamics is presented in Bulíček et al. (2019). Loeffel and Anand (2011) have developed a thermo–chemo–mechanical theory for diffusion of chemically reacting species in finitely deforming materials. These works were applied to study problems in elastomeric gels (Chester and Anand, 2011; Chester et al., 2015). In a series of papers, Masud and coworkers (Gajendran et al., 2018; Anguiano and Masud, 2021) have presented advanced numerical methods for modeling thermo–chemo–mechanical processes in multi-constituent materials. These models were extended for application to open systems comprised of nonlinear elastic solids that are infused with reactive fluids and are undergoing large local strains (Anguiano et al., 2022).

This paper develops a thermo–chemo–mechanical model from the fundamental physical laws satisfying: (i) balance of momentum, (ii) balance of energy, and (iii) the second law of thermodynamics. The curing of the material is modeled as an energy dissipation process that causes micromechanic changes resulting in evolving material parameters. We show that the second law of thermodynamics implies the existence of an inelastic process that is associated with material evolution due to curing. This inelastic process results in permanent deformation which has been observed in experimental investigations with FP that are reported in Kumar et al. (2022). Employing an internal variable formalism we model the inelastic process and derive the evolution equation for the internal variable.

The reactive and thermal processes in the curing of the material often lead to large local deformations together with the internal stresses that develop as a consequence. Therefore, it is important to develop constitutive equations that are not only thermodynamically consistent, but can also accommodate finite strains. Embedding these constitutive equations in the balance laws result in mixed-field formulations for the coupled response in the nonlinear regime. Mixed field formulations require special treatment, and in the context of finite elements, they are governed by the theory of mixed finite element methods (Brezzi and Fortin, 1991). The class of stabilized methods provides appropriate variational frameworks to develop mathematically robust numerical methods for mixed-field problems. Stabilized methods bypass the classical *inf-sup* condition for mixed problems, thereby facilitating the use of arbitrary combinations of interpolation functions to approximate the various unknown fields. Since the resulting methods are fully coupled at the variational level, this provides an opportunity to develop monolithic solution algorithms wherein all the fields are solved concurrently, and without the need to resort to staggered solution techniques that are invariably limited to only first-order accuracy.

An outline of the paper is as follows. Section 2 presents the constitutive model which is developed in the context of finite strain kinematics. A stabilized numerical method is presented in Section 3. Section 4 presents a set of numerical test cases for the validation of the model, and the application of the method to some interesting problem classes. Concluding remark are given in Section 5.

2. Thermo–chemo–mechanical formulation in finite deformation

The proposed FP model consists of three coupled components: (i) polymerization, (ii) heat transfer, and (iii) mechanical deformation. Curing is initiated by heat supply to a polymer body that locally increases the temperature and starts the process of polymerization. Subsequently, the exothermic curing process itself generates heat that results in self-sustained propagation of the polymerization front. This traveling front that separates material that has polymerized from the yet untransformed material leads to local thermal-expansion and cure-shrinkage in addition to evolution of the material properties in the newly formed material.

This section presents a model for FP that is developed from fundamental physical laws of balance of momentum, balance of energy, and the second law of thermodynamics. To be able to model material and geometric instabilities that can get triggered during DIW with FP processes, the formulation is developed in the context of finite deformation kinematics.

2.1. Kinematics

Consider a body that at time $t = 0$ occupies an open bounded domain $\Omega_0 \subset \mathbb{R}^{n_{sd}}$ with boundary $\partial\Omega_0$, where n_{sd} is the number of spatial dimensions. The material points in the initial configuration are denoted by $\mathbf{X} \in \Omega_0$. In response to mechanical and thermal loading, the material point $\mathbf{X}$ moves to $\mathbf{x} \in \Omega_t \subset \mathbb{R}^{n_{sd}}$ at time $t \in (0, T]$. This motion is described by a one-to-one deformation map $\boldsymbol{\varphi} : \Omega_0 \to \Omega_t$ such that

$$\mathbf{x} = \boldsymbol{\varphi}(\mathbf{X}, t). \tag{1}$$

The displacement field is denoted by $\mathbf{u}$ and is defined as

$$\mathbf{u}(\mathbf{X}, t) = \boldsymbol{\varphi}(\mathbf{X}, t) - \mathbf{X}. \tag{2}$$

The deformation map is assumed to be sufficiently smooth such that the deformation gradient and its Jacobian can be defined as

$$\mathbf{F} = \nabla\boldsymbol{\varphi} = \frac{\partial\boldsymbol{\varphi}}{\partial\mathbf{X}} = \mathbf{I} + \frac{\partial\mathbf{u}}{\partial\mathbf{X}}, \tag{3}$$

$$J = \det \mathbf{F}, \tag{4}$$

where $\nabla\boldsymbol{\varphi}$ is the gradient of the deformation map and $\mathbf{I}$ is the identity tensor. The velocity field can be defined in terms $\mathbf{X}$ from the deformation map or the displacement field.

$$\mathbf{V} = \frac{\partial\boldsymbol{\varphi}}{\partial t} = \frac{\partial\mathbf{u}}{\partial t}. \tag{5}$$

Let $\boldsymbol{\varphi}_t(\mathbf{X})$ be the mapping $\boldsymbol{\varphi}(\mathbf{X}, t)$ at a given but otherwise arbitrary time t. The velocity field can also be written in terms of $\mathbf{x}$ via inverse of the deformation map as

$$\mathbf{v}(\mathbf{x}, t) = \mathbf{V}(\boldsymbol{\varphi}_t^{-1}(\mathbf{x}), t). \tag{6}$$

For an arbitrary field $A(\mathbf{X}, t) = a(\boldsymbol{\varphi}_t(\mathbf{X}), t)$, the material time derivative in the Lagrangian and Eulerian frame is defined as

$$\dot{A} = \frac{DA}{Dt} = \frac{\partial A}{\partial t}, \qquad \dot{a} = \frac{Da}{Dt} = \frac{\partial A}{\partial t} = \frac{\partial a}{\partial t} + \mathbf{v} \cdot \frac{\partial a}{\partial \mathbf{x}}. \tag{7}$$

2.2. Balance equations

All thermodynamics processes are required to satisfy the balance of linear momentum

$$\text{Div } \mathbf{P} - \mathbf{B} = \mathbf{0}, \tag{8}$$

and the balance of energy

$$\rho_0 \dot{E} + \nabla \cdot \mathbf{Q} - \mathbf{P} : \dot{\mathbf{F}} - \rho_0 R - C_\gamma \dot{\gamma} = 0, \tag{9}$$

where $\mathbf{P}$ is the first Piola–Kirchhoff stress tensor, $\mathbf{B}$ is the body force vector, ρ_0 is the mass per unit volume in the reference configuration, E is the specific internal energy per unit mass, $\mathbf{Q}$ is the heat flux vector, $\nabla \cdot \mathbf{Q}$ is the divergence of $\mathbf{Q}$, R is the heat source, and γ is the degree of cure, The last term in (9) represents the chemical power that accounts for the change of internal energy due to the breaking and formation of chemical bonds. For completeness, it is noted that the balance of angular momentum can be satisfied by providing a symmetric Cauchy stress tensor $\boldsymbol{\sigma} = J^{-1}\mathbf{P}\mathbf{F}^T$.

2.3. Constitutive restriction from the second law of thermodynamics

The second law of thermodynamics puts restriction on the constitutive relations (Coleman and Noll, 1963). In the context of internal variable formalism, the temporal evolution of these variables should be such that the second law is satisfied (Coleman and Gurtin, 1967). In the following developments, two internal variables are used: degree of cure γ, and inelastic Cauchy–Green deformation tensor $\mathbf{C}^i$. We consider the second law at the continuum scale in the form of the Clausius–Duhem inequality.

$$\rho_0 \dot{N} + \nabla \cdot \left(\frac{\mathbf{Q}}{\Theta}\right) - \frac{\rho_0 R}{\Theta} - \frac{C_\gamma}{\Theta}\dot{\gamma} \geq 0, \tag{10}$$

where N is the specific entropy per unit mass, Θ is the absolute temperature, R is the heat source, and C_γ is a parameter associated with the heat generated by the exothermic curing process. Multiplying (10) by Θ and substituting (9) yields

$$\rho_0\left(\Theta\dot{N}-\dot{E}\right)-\frac{\mathbf{Q}\cdot\nabla\Theta}{\Theta}+\mathbf{P}:\dot{\mathbf{F}}\geq 0. \tag{11}$$

Next, we consider internal energy and specific entropy functions of the following form

$$E(\mathbf{F},\mathbf{C}^i,\Theta,\gamma),\qquad N(\mathbf{F},\mathbf{C}^i,\Theta,\gamma). \tag{12}$$

Let $\Psi(\mathbf{F},\mathbf{C}^i,\Theta,\gamma)$ be the specific Helmholtz free energy function written in the reference configuration, and defined as

$$\Psi=E-\Theta N. \tag{13}$$

Substituting (13) in the inequality (11) yields the Reduced Dissipation Inequality (RDI)

$$\mathcal{D}=-\rho_0\left(\dot{\Psi}+N\dot{\Theta}\right)-\frac{\mathbf{Q}\cdot\nabla\Theta}{\Theta}+\mathbf{P}:\dot{\mathbf{F}}\geq 0, \tag{14}$$

where $\mathcal{D}$ is the total energy dissipation. Taking material time derivative of Ψ and rearranging the terms yields

$$\mathcal{D}=-\rho_0\left(\frac{\partial\Psi}{\partial\Theta}+N\right)\dot{\Theta}-\left(\rho_0\frac{\partial\Psi}{\partial\mathbf{F}}-\mathbf{P}\right):\dot{\mathbf{F}}-\rho_0\left(\frac{\partial\Psi}{\partial\mathbf{C}^i}:\dot{\mathbf{C}}^i+\frac{\partial\Psi}{\partial\gamma}\dot{\gamma}\right)-\frac{\mathbf{Q}\cdot\nabla\Theta}{\Theta}\geq 0. \tag{15}$$

The inequality (15) is satisfied by enforcing the following relations.

$$\begin{aligned}
\text{Entropy:}\qquad & N=-\frac{\partial\Psi}{\partial\Theta},\\
\text{Stress:}\qquad & \mathbf{P}=\rho_0\frac{\partial\Psi}{\partial\mathbf{F}},\\
\text{Inelasticity in material evolution:}\qquad & -\frac{\partial\Psi}{\partial\mathbf{C}^i}:\dot{\mathbf{C}}^i-\frac{\partial\Psi}{\partial\gamma}\dot{\gamma}\geq 0,\\
\text{Heat flux:}\qquad & -\frac{\mathbf{Q}\cdot\nabla\Theta}{\Theta}\geq 0.
\end{aligned} \tag{16}$$

where the last two inequalities describe the dissipation processes. At this point, one can develop constitutive equations either in entropy form or in the temperature form.

Remark 1. The focus of the current paper is the inelastic strain associated with the material evolution. To keep the discussion simple, we have opted not to include cure shrinkage in this work. Inclusion of cure shrinkage to the model can be done by adding an internal variable associated with it, wherein the evolution equation will need to satisfy the second law of thermodynamics while conforming to the experimentally observed behavior of the material.

2.4. Temperature form of balance of energy

Since our objective is to develop a thermomechanical formulation wherein the thermal field directly feeds into the chemical curing model, we write the balance of energy in terms of temperature instead of entropy. Solving for the stress power term $\mathbf{P}:\dot{\mathbf{F}}$ in (14) and substituting it in the balance of energy (9) gives

$$\rho_0\left(\dot{E}-\dot{\Psi}-N\dot{\Theta}\right)+\nabla\cdot\mathbf{Q}-\rho_0 R-C_\gamma\dot{\gamma}-\frac{\mathbf{Q}\cdot\nabla\Theta}{\Theta}-\mathcal{D}=0. \tag{17}$$

Using (13) and ((16)-1),

$$-\rho_0\frac{D}{Dt}\left[\frac{\partial\Psi}{\partial\Theta}\right]+\nabla\cdot\mathbf{Q}-\rho_0 R-C_\gamma\dot{\gamma}-\frac{\mathbf{Q}\cdot\nabla\Theta}{\Theta}-\mathcal{D}=0. \tag{18}$$

Computing the material time derivative of $\partial\Psi/\partial\Theta$ and substituting (15) and (16) into (18), we obtain the balance of energy in the temperature form as

$$-\rho_0 C_\Theta\dot{\Theta}+\nabla\cdot\mathbf{Q}-\rho_0 R-C_\gamma\dot{\gamma}+\mathcal{H}_{EI}-\mathcal{D}_{int}=0, \tag{19}$$

where C_Θ is the specific heat, $\mathcal{H}_{EI}$ is the elastic–inelastic structural heating, and $\mathcal{D}_{int}$ is the internal dissipation given as follows:

$$C_\Theta=-\Theta\frac{\partial^2\Psi}{\partial\Theta^2}, \tag{20}$$

$$\mathcal{H}_{EI}=-\rho_0\Theta\frac{\partial^2\Psi}{\partial\Theta\partial\mathbf{F}}:\dot{\mathbf{F}}-\rho_0\Theta\frac{\partial^2\Psi}{\partial\Theta\partial\mathbf{C}^i}:\dot{\mathbf{C}}^i-\rho_0\Theta\frac{\partial^2\Psi}{\partial\Theta\partial\gamma}\dot{\gamma}, \tag{21}$$

$$\mathcal{D}_{int}=-\rho_0\left(\frac{\partial\Psi}{\partial\mathbf{C}^i}:\dot{\mathbf{C}}^i+\frac{\partial\Psi}{\partial\gamma}\dot{\gamma}\right). \tag{22}$$

2.5. Constitutive equations

We employ the Helmholtz free energy function of the following form to model evolving materials that are used in FP process:

$$\rho_0\Psi(\mathbf{E},\mathbf{E}^i,\Theta,\gamma) = \frac{1}{2}\kappa(\gamma)\mathrm{tr}[\mathbf{E}^e]^2 + \mu(\gamma)\left(\mathrm{tr}[(\mathbf{E}^e)^2] - \frac{1}{3}\mathrm{tr}[\mathbf{E}^e]^2\right) + \rho_0 C_\Theta\left[(\Theta-\Theta_{\mathrm{ref}}) - \Theta\ln\left(\frac{\Theta}{\Theta_{\mathrm{ref}}}\right)\right], \tag{23}$$

where the elastic strain $\mathbf{E}^e$ is defined in terms of total strain $\mathbf{E}$, inelastic strain $\mathbf{E}^i$, and thermal strain $\mathbf{E}^\Theta$ as follows.

$$\mathbf{E}^e = \mathbf{E} - \mathbf{E}^i - \mathbf{E}^\Theta, \tag{24}$$

$$\mathbf{E} = \frac{1}{2}(\mathbf{C}-\mathbf{I}), \qquad \mathbf{E}^i = \frac{1}{2}(\mathbf{C}^i-\mathbf{I}), \qquad \mathbf{E}^\Theta = \alpha\mathbf{I}(\Theta-\Theta_{\mathrm{ref}}), \tag{25}$$

where $\mathbf{C} = \mathbf{F}^T\mathbf{F}$ is the right Cauchy–Green deformation tensor, and the reference temperature Θ_{ref} is the temperature where thermal strain $\mathbf{E}^\Theta = 0$. The specific heat C_Θ and the coefficient of thermal expansion α are constants while the bulk modulus $\kappa(\gamma)$ and the shear modulus $\mu(\gamma)$ are a function of the degree of cure γ that account for the curing of the material. The degree of cure is given by a curing model of the following form:

$$\dot{\gamma} = f(\Theta,\gamma) \geq 0. \tag{26}$$

Following ((16)-2) and using the relation $\mathbf{P} = \mathbf{F}\mathbf{S}$, the second Piola–Kirchhoff stress tensor is given as

$$\mathbf{S} = \kappa(\gamma)\,\mathrm{tr}[\mathbf{E}^e]\mathbf{I} + 2\mu(\gamma)\left(\mathbf{E}^e - \frac{1}{3}\mathrm{tr}[\mathbf{E}^e]\mathbf{I}\right). \tag{27}$$

To model the relation between heat flux and temperature, a spatially isotropic Fourier law (Wcisło et al., 2023) is used.

$$\mathbf{Q} = -kJ\mathbf{C}^{-1}\nabla\Theta \tag{28}$$

where $k > 0$ is the thermal conductivity measured in the spatial or eulerian configuration. Using positive definiteness of $\mathbf{C}$, it is straightforward to show that (28) satisfies the thermodynamic constraint ((16)-4).

2.6. Inelasticity in material evolution

It has been shown that evolution of material parameters for modeling stiffening effect in a purely elastic materials results in the violation of the second law of thermodynamics, both in the small deformation formulations (Bažant, 1979; Bažant et al., 1988) as well as in the finite deformation formulations (Wijaya et al., 2022). The second law implies that there must be a dissipation process during material evolution which can lead to permanent deformation that gets frozen in the morphology of the material as it cures. This finding is consistent with the experimental observations in Kumar et al. (2022) and Kumar et al. (2024) that has reported "irreversible freezing of deformation associated with FP". To model this behavior of the material, we begin by taking total time derivative of $\mathbf{S}$:

$$\dot{\mathbf{S}} = \frac{\partial\mathbf{S}}{\partial\mathbf{E}} : \dot{\mathbf{E}} + \frac{\partial\mathbf{S}}{\partial\mathbf{E}^i} : \dot{\mathbf{E}}^i + \frac{\partial\mathbf{S}}{\partial\gamma}\dot{\gamma} + \frac{\partial\mathbf{S}}{\partial\Theta}\dot{\Theta}. \tag{29}$$

We postulate that the evolution equation for $\mathbf{E}^i$ satisfies the following relation:

$$\dot{\mathbf{S}} = \frac{\partial\mathbf{S}}{\partial\mathbf{E}} : \dot{\mathbf{E}} + \frac{\partial\mathbf{S}}{\partial\Theta}\dot{\Theta}. \tag{30}$$

which is the rate form of constitutive relation for an elastic material in a thermomechanical setting. This form is recommended in Bažant (1979) and Bažant et al. (1988). Flow rule that satisfies (30) has been applied to constitutive models for cementitious materials in Wijaya et al. (2022) and Wijaya et al. (2024). Subtracting (30) from (29), we obtain the relation between the two internal variables:

$$0 = \frac{\partial\mathbf{S}}{\partial\mathbf{E}^i} : \dot{\mathbf{E}}^i + \frac{\partial\mathbf{S}}{\partial\gamma}\dot{\gamma} \tag{31}$$

Solving for $\mathbf{E}^i$ in (31) gives the evolution equation

$$\dot{\mathbf{E}}^i = \frac{\kappa'(\gamma)\dot{\gamma}}{3\kappa(\gamma)}\mathrm{tr}[\mathbf{E}^e]\mathbf{I} + \frac{\mu'(\gamma)\dot{\gamma}}{\mu(\gamma)}\left(\mathbf{E}^e - \frac{1}{3}\mathrm{tr}[\mathbf{E}^e]\mathbf{I}\right). \tag{32}$$

Using this evolution equation, the internal dissipation can be computed.

$$\mathcal{D}_{int} = -\rho_0\left(\frac{\partial\Psi}{\partial\mathbf{C}^i} : \dot{\mathbf{C}}^i + \frac{\partial\Psi}{\partial\gamma}\dot{\gamma}\right) = \rho_0\frac{\partial\Psi}{\partial\gamma}\dot{\gamma}. \tag{33}$$

For stiffening material, $\dot{\gamma} \geq 0$, $\kappa' \geq 0$, and $\mu' \geq 0$. In this case, $\mathcal{D}_{int} \geq 0$. This shows that the flow rule obtained by enforcing (30) satisfies the second law of thermodynamics. The derivation of (32) and (33) is given in Appendix. The thermo–chemo–mechanical constitutive model is summarized in Box I.

Remark 2. It is important to note that besides (30) there may be other choices for postulating the evolution of $\mathbf{E}^i$ that can satisfy the second law of thermodynamics. However, enforcing (30) is equivalent to using rate form of the constitutive model for stress update. This leads to a model that behaves as discussed in Wijaya et al. (2022).

Remark 3. One may choose to use the rate form of the constitutive relation (such as (30)) to carry out stress update instead of using the flow rule (32) in direct form (Bažant, 1979; Bažant et al., 1988). If the rate form is used, special care needs to be taken to ensure that the stress rate is objective (Simo and Hughes, 1998). Some examples of objective stress rate are Jaumann–Zaremba and Green–McInnis–Naghdi stress rate. Nedjar (2021, 2022) present some examples on how to deal with the evolving material parameters using the rate form of the constitutive relations. Whether the rate form or the evolution equation is used, in either case the resulting model is inelastic.

Remark 4. The evolution Eq. (32) in direct form is much simpler to use as compared to the rate form. It will be shown in the subsequent section that if the constitutive relation is invertible, the internal variable can be computed analytically. It is also relatively straightforward to combine the inelasticity arising from material evolution with other sources of inelasticity such as viscoelasticity and plasticity.

2.7. The initial boundary value problem

In the context of FP, one can assume that the elastic–inelastic structural heating $\mathcal{H}_{EI}$ and the internal dissipation $\mathcal{D}_{int}$ are negligible compared to the heat produced by the curing process $C_\gamma \dot{\gamma}$. We also assume that there are no heat sources other than the energy released from the exothermic polymer curing reaction. Lastly, to keep the problem simple, all Neumann boundary conditions are assumed homogeneous. The initial–boundary–value problem is comprised of the following sets of equations:

(i) Balance of linear momentum:

$$\begin{aligned}
&\mathrm{Div}\,\mathbf{P} - \mathbf{B} = \mathbf{0} && \forall (\mathbf{X},t) \in \Omega_0 \times [0,T],\\
&\boldsymbol{\varphi}(\mathbf{X},t) = \overline{\boldsymbol{\varphi}}(\mathbf{X},t) && \forall (\mathbf{X},t) \in \partial\Omega_0^{\mathcal{D}_\varphi} \times [0,T],\\
&\mathbf{P}(\mathbf{X},t)\mathbf{N} = \mathbf{0} && \forall (\mathbf{X},t) \in \partial\Omega_0^{\mathcal{N}_\varphi} \times [0,T],\\
&\boldsymbol{\varphi}(\mathbf{X},0) = \mathbf{0} && \forall \mathbf{X} \in \Omega_0;
\end{aligned} \tag{34}$$

(ii) Balance of energy:

$$\begin{aligned}
&\rho_0 C_\Theta \dot{\Theta} + \nabla \cdot \mathbf{Q} - C_\gamma \dot{\gamma} = 0 && \forall (\mathbf{X},t) \in \Omega_0 \times [0,T],\\
&\Theta(\mathbf{X},t) = \overline{\Theta}(\mathbf{X},t) && \forall (\mathbf{X},t) \in \partial\Omega_0^{\mathcal{D}_\Theta} \times [0,T],\\
&\mathbf{Q}(\mathbf{X},t)\cdot\mathbf{N} = \mathbf{0} && \forall (\mathbf{X},t) \in \partial\Omega_0^{\mathcal{N}_\Theta} \times [0,T],\\
&\mathbf{Q}(\mathbf{X},t) = H_\Theta(\Theta(\mathbf{X},t) - \Theta_\infty) && \forall (\mathbf{X},t) \in \partial\Omega_0^{\mathcal{R}_\Theta} \times [0,T],\\
&\Theta(\mathbf{X},0) = \Theta_0(\mathbf{X}) && \forall \mathbf{X} \in \Omega_0;
\end{aligned} \tag{35}$$

(iii) Evolution equation for the cure kinetics:

$$\begin{aligned}
&\dot{\gamma}(\mathbf{X},t) = f(\Theta,\gamma) && \forall (\mathbf{X},t) \in \Omega_0 \times [0,T],\\
&\gamma(\mathbf{X},0) = \gamma_0(\mathbf{X}) && \forall \mathbf{X} \in \Omega_0;
\end{aligned} \tag{36}$$

(iv) Evolution equation for the inelastic strain:

$$\begin{aligned}
&\dot{\mathbf{E}}^i(\mathbf{X},t) = \frac{\kappa'(\gamma)\dot{\gamma}}{3\kappa(\gamma)}\mathrm{tr}[\mathbf{E}^e]\mathbf{I} + \frac{\mu'(\gamma)\dot{\gamma}}{\mu(\gamma)}\left(\mathbf{E}^e - \frac{1}{3}\mathrm{tr}[\mathbf{E}^e]\mathbf{I}\right) && \forall (\mathbf{X},t) \in \Omega_0 \times [0,T],\\
&\mathbf{E}^i(\mathbf{X},0) = \mathbf{E}^i_0(\mathbf{X}) && \forall \mathbf{X} \in \Omega_0;
\end{aligned} \tag{37}$$

where H_Θ is the heat transfer coefficient between the body and the environment. Superscript $\mathcal{D}_\mathcal{F}, \mathcal{N}_\mathcal{F}, \mathcal{R}_\mathcal{F}$ denote Dirichlet, Neumann, and Robin parts of the boundary with respect to the solution field $\mathcal{F} \in \{\boldsymbol{\varphi}, \Theta\}$. The initial value for the inelastic strain is considered zero, i.e., $\mathbf{E}^i_0 = \mathbf{0}$.

3. Stabilized mixed finite element method for the initial boundary value problem

Since FP involves multiple interacting fields, namely, displacement, temperature, curing, and inelastic strain, it results in coupled mixed-field formulations. Numerical methods for nonlinear mixed-field formulations need enhanced stability to accurately resolve the nonlinearly evolving fields. In this work we have employed a stabilization technique (Hughes, 1995; Masud, 2004) that is based on Variational Multiscale (VMS) method for finite strain formulations proposed in Masud and Truster (2013). The VMS stabilization has shown success in phase evolution problems (Masud and Xia, 2006), and has also been used in various applications namely: (i) heat transfer (Ayub and Masud, 2003; Masud and Kwack, 2008), (ii) interface mechanics (Truster et al., 2015), and (iii) problem with material evolution and traveling curing fronts (Masud et al., 2020; Anguiano et al., 2020). The hierarchical modeling feature in VMS framework facilitates the development of residual-based closure models of fine-scale physics (Masud and Franca, 2008). These closure models represent features in the solution that may be beyond the modeling capability of the basis functions that are employed to approximate the unknown fields, or there are features that are beyond the resolution capability of the numerical discretization used. Implicitly accounting for this missing physics by embedding the residual-based closure models in the variational formulations not only enhances the stability of the resulting method, it also increases the accuracy of the computed physics.

The enhanced stability of the mixed field formulation helps with the classical *inf-sup* condition that restricts the use of arbitrary combination of interpolation function for the various unknown fields (Brezzi and Fortin, 1991). Because of this increased stability,

1. Free energy function:

$$\rho_0\Psi(\mathbf{E},\mathbf{E}^i,\Theta,\gamma) = \frac{1}{2}\kappa(\gamma)\mathrm{tr}[\mathbf{E}^e]^2 + \mu(\gamma)\left(\mathrm{tr}[(\mathbf{E}^e)^2] - \frac{1}{3}\mathrm{tr}[\mathbf{E}^e]^2\right) + \rho_0 C_\Theta\left[(\Theta-\Theta_{\mathrm{ref}}) - \Theta\ln\left(\frac{\Theta}{\Theta_{\mathrm{ref}}}\right)\right],$$

where

$$\mathbf{E}^e = \mathbf{E} - \mathbf{E}^i - \mathbf{E}^\Theta,$$

$$\mathbf{E} = \frac{1}{2}(\mathbf{C}-\mathbf{I}), \qquad \mathbf{E}^i = \frac{1}{2}(\mathbf{C}^i - \mathbf{I}), \qquad \mathbf{E}^\Theta = \alpha\mathbf{I}(\Theta - \Theta_{\mathrm{ref}}).$$

2. First Piola–Kirchhoff stress and entropy:

$$\mathbf{P} = \rho_0\frac{\partial\Psi}{\partial\mathbf{F}}, \qquad N = -\frac{\partial\Psi}{\partial\Theta},$$

3. Evolution equations for the degree of cure and the inelastic strain:

$$\dot\gamma = f(\Theta,\gamma) \ge 0,$$

$$\dot{\mathbf{E}}^i = \frac{\kappa'(\gamma)\dot\gamma}{3\kappa(\gamma)}\mathrm{tr}[\mathbf{E}^e]\mathbf{I} + \frac{2\mu'(\gamma)\dot\gamma}{2\mu(\gamma)}\left(\mathbf{E}^e - \frac{1}{3}\mathrm{tr}[\mathbf{E}^e]\mathbf{I}\right).$$

4. Capacity, elastic–inelastic heating, internal dissipation, heat flux:

$$C_\Theta = -\Theta\frac{\partial^2\Psi}{\partial\Theta^2},$$

$$\mathcal{H}_{EI} = -\rho_0\Theta\frac{\partial^2\Psi}{\partial\Theta\partial\mathbf{F}} : \dot{\mathbf{F}} - \rho_0\Theta\frac{\partial^2\Psi}{\partial\Theta\partial\mathbf{C}^i} : \dot{\mathbf{C}}^i - \rho_0\Theta\frac{\partial^2\Psi}{\partial\Theta\partial\gamma}\dot\gamma,$$

$$\mathcal{D}_{int} = \rho_0\frac{\partial\Psi}{\partial\gamma}\dot\gamma,$$

$$\mathbf{Q} = -kJ\mathbf{C}^{-1}\nabla\Theta$$

Box I. Thermo–chemo–mechanical constitutive model.

we are able to use equal order Lagrange polynomials, e.g. 8-node hexahedral elements for the displacement and temperature fields (Masud and Chen, 2019).

Another significant attribute of the stabilized method is that it allows concurrent solution of the various coupled fields in a monolithic manner, and therefore eliminates the need to resort to staggered solution algorithms that have traditionally been employed in the literature (Armero and Simo, 1992; Simo and Miehe, 1992). Since stabilized formulation is systematically derived, it lends itself to consistent linearization that yields quadratic rate of convergence of the solution in the Newton–Raphson method.

3.1. Weak form of the governing equations

We write the weak form of (34) and (35) in the residual form. Find $(\boldsymbol{\varphi},\Theta)\in\mathcal{S}\times\mathcal{Q}$ such that $\forall(\boldsymbol{\eta},w)\in\mathcal{V}\times\mathcal{P}$,

$$R_{\boldsymbol{\varphi}}(\boldsymbol{\eta},\boldsymbol{\varphi},\Theta,\gamma,\mathbf{E}^i) \equiv \int_{\Omega_0}\nabla\boldsymbol{\eta}\cdot\mathbf{P}\,\mathrm{d}\mathbf{X} - \int_{\Omega_0}\boldsymbol{\eta}\cdot\mathbf{B}\,\mathrm{d}\mathbf{X} = 0, \tag{38}$$

$$\begin{aligned} R_\Theta(w,\boldsymbol{\varphi},\Theta,\gamma,\mathbf{E}^i) \equiv{}& \int_{\Omega_0} w\rho_0 C_\Theta\dot\Theta\,\mathrm{d}\mathbf{X} + \int_{\Omega_0}\nabla w\cdot\mathbf{Q}\,\mathrm{d}\mathbf{X} - \int_{\Omega_0} wC_\gamma\dot\gamma\,\mathrm{d}\mathbf{X} \\ &+ \int_{\partial\Omega_0^{\mathcal{R}_\Theta}} wH_\Theta(\Theta-\Theta_\infty)\,\mathrm{d}\mathbf{X} = 0. \end{aligned} \tag{39}$$

where γ is defined by (36), $\mathbf{E}^i$ is defined by (32), and the function spaces are defined as follows:

$$\begin{aligned} &\mathcal{S} = \{\boldsymbol{\varphi}_t(\mathbf{X})\in H^1(\Omega_0) : \boldsymbol{\varphi} = \overline{\boldsymbol{\varphi}} \text{ for } \mathbf{X}\in\partial\Omega_0^{\mathcal{D}_\varphi}\}, \quad \mathcal{V} = \{\boldsymbol{\eta}_t(\mathbf{X})\in H^1(\Omega_0) : \boldsymbol{\eta} = 0 \text{ for } \mathbf{X}\in\partial\Omega_0^{\mathcal{D}_\varphi}\}, \\ &\mathcal{Q} = \{\Theta_t(\mathbf{X})\in H^1(\Omega_0) : \Theta = \overline{\Theta} \text{ for } \mathbf{X}\in\partial\Omega_0^{\mathcal{D}_\Theta}\}, \quad \mathcal{P} = \{w_t(\mathbf{X})\in H^1(\Omega_0) : w = 0 \text{ for } \mathbf{X}\in\partial\Omega_0^{\mathcal{D}_\Theta}\}. \end{aligned} \tag{40}$$

where $\boldsymbol{\varphi}_t(\mathbf{X}) = \boldsymbol{\varphi}(\mathbf{X},t), \boldsymbol{\eta}_t(\mathbf{X}) = \boldsymbol{\eta}(\mathbf{X},t), \Theta_t(\mathbf{X}) = \Theta(\mathbf{X},t)$ and $w_t(\mathbf{X}) = w(\mathbf{X},t)$. For further elaboration on these spaces of functions, see Brezzi and Fortin (1991).

3.2. A stabilized weak form derived via the variational multiscale (VMS) method

To derive the VMS stabilized form, we consider a decomposition of the deformation map into the coarse-scale map $\hat{\boldsymbol{\varphi}}$ and fine-scale map $\tilde{\boldsymbol{\varphi}}$. It can also be written in terms of coarse-scale displacement $\hat{\mathbf{u}}$ and fine-scale displacement $\tilde{\mathbf{u}}$ as

$$\boldsymbol{\varphi} = \tilde{\boldsymbol{\varphi}} \circ \hat{\boldsymbol{\varphi}} = \mathbf{X} + \hat{\mathbf{u}} + \tilde{\mathbf{u}}. \tag{41}$$

The coarse-scale map represents part of the deformation field that belongs to the approximation space while the fine-scale map represents the error of the approximation and can be considered as part of the physics that is higher-order or finer and therefore beyond the resolution capability of the discretization and that of the functional spaces employed for the coarse scales. The deformation gradient can be computed from the decomposition as

$$\mathbf{F} = \frac{\partial \boldsymbol{\varphi}}{\partial \mathbf{X}} = \frac{\partial \tilde{\boldsymbol{\varphi}}}{\partial \boldsymbol{\zeta}} \frac{\partial \hat{\boldsymbol{\varphi}}}{\partial \mathbf{X}} = \tilde{\mathbf{F}}\hat{\mathbf{F}}, \tag{42}$$

where $\boldsymbol{\zeta} = \hat{\boldsymbol{\varphi}}(\mathbf{X}, t)$ can be viewed as an intermediate configuration. $\hat{\mathbf{F}}$ and $\tilde{\mathbf{F}}$ are the coarse-scale and fine-scale deformation gradients. We make use of the coarse-scale and fine-scale maps to decompose the weight function

$$\boldsymbol{\eta} = \underbrace{\tilde{\boldsymbol{\varphi}} \circ \hat{\boldsymbol{\eta}}}_{\hat{\boldsymbol{\eta}}_{\tilde{\boldsymbol{\varphi}}}} + \underbrace{\tilde{\boldsymbol{\eta}} \circ \hat{\boldsymbol{\varphi}}}_{\tilde{\boldsymbol{\eta}}_{\hat{\boldsymbol{\varphi}}}} \tag{43}$$

into a coarse-scale part $\hat{\boldsymbol{\eta}}$ and a fine-scale part $\tilde{\boldsymbol{\eta}}$. Following Masud and Chen (2019), we apply the notion of stabilization only to the balance of linear momentum (38), and therefore split only the displacement field into coarse and fine parts via the compositional mapping in (41).

The derivation of the stabilized method is comprised of two steps: Employing the arbitrariness of the decomposed weight function (43), we split the multiscale weak form into coarse- and fine-scale weak forms. Subsequently, with suitable assumptions imposed on the fine-scale field (Masud and Truster, 2013; Masud and Chen, 2019), we locally resolve the fine-scale subproblem and extract the fine-scale solution. This derived fine-scale field can also be considered as the closure model for the part of physics that is missing due to the limitation of the allowable space of functions used for the coarse scales to approximate higher order effects in the solution.

Accordingly, substituting (42) and (43) into (38), we obtained the following two subproblems:

Coarse-scale subproblem

$$\hat{R}_{\boldsymbol{\varphi}}(\hat{\boldsymbol{\eta}}, \tilde{\boldsymbol{\varphi}}, \hat{\boldsymbol{\varphi}}, \Theta, \gamma, \mathbf{E}^i) \equiv \int_{\Omega} (\tilde{\mathbf{F}} \cdot \nabla \hat{\boldsymbol{\eta}}) \cdot \mathbf{P} \, \mathrm{d}\mathbf{X} - \int_{\Omega} \hat{\boldsymbol{\eta}}_{\tilde{\boldsymbol{\varphi}}} \cdot \mathbf{B} \, \mathrm{d}\mathbf{X} = 0. \tag{44}$$

Fine-scale subproblem

$$\tilde{R}_{\boldsymbol{\varphi}}(\tilde{\boldsymbol{\eta}}, \tilde{\boldsymbol{\varphi}}, \hat{\boldsymbol{\varphi}}, \Theta, \gamma, \mathbf{E}^i) \equiv \int_{\Omega} \nabla \tilde{\boldsymbol{\eta}} \cdot \mathbf{P} \, \mathrm{d}\mathbf{X} - \int_{\Omega} \tilde{\boldsymbol{\eta}}_{\hat{\boldsymbol{\varphi}}} \cdot \mathbf{B} \, \mathrm{d}\mathbf{X} = 0. \tag{45}$$

We linearize the fine-scale and coarse-scale problems around $\tilde{\mathbf{u}} = \mathbf{0}$. The linearization is consistent with the interpretation of fine-scales as error of the coarse-scale approximation. The fine-scale solution is substituted in the linearized coarse-scale formulation to obtain the stabilized form. These steps are presented in detail in Masud and Truster (2013). The final stabilized form is

$$R_{\boldsymbol{\varphi}}^{\mathrm{stab}}(\boldsymbol{\eta}, \boldsymbol{\varphi}, \Theta, \gamma, \mathbf{E}^i) \equiv \int_{\Omega_0} \mathbf{S} \cdot \delta \mathbf{E}(\boldsymbol{\eta}) \, \mathrm{d}\mathbf{X} - \int_{\Omega_0} \boldsymbol{\eta} \cdot \mathbf{B} \, \mathrm{d}\mathbf{X} - S_{\boldsymbol{\varphi}}(\boldsymbol{\eta}, \boldsymbol{\varphi}, \Theta, \gamma) = 0, \tag{46}$$

with stabilization terms

$$S_{\boldsymbol{\varphi}}(\boldsymbol{\eta}, \boldsymbol{\varphi}, \Theta, \gamma, \mathbf{E}^i) = \int_{\Omega_0} \left(\mathrm{Div}\left[\nabla \boldsymbol{\eta} \mathbf{S} + \mathbf{F}(\boldsymbol{C} : \delta \mathbf{E}(\boldsymbol{\eta}))\right]\right) \cdot \boldsymbol{\tau}_{\Omega} \hat{\mathbf{R}} \, \mathrm{d}\mathbf{X}, \tag{47}$$

where

$$\boldsymbol{C} = 4\partial^2 \psi / \partial \mathbf{C} \partial \mathbf{C}, \tag{48}$$

$$\delta \mathbf{E}(\boldsymbol{\eta}_0) = 1/2(\nabla \boldsymbol{\varphi}^{\alpha,T} \nabla \boldsymbol{\eta} + \nabla \boldsymbol{\eta}^{\alpha,T} \nabla \boldsymbol{\varphi}), \tag{49}$$

with the coarse-scale residual and the stabilization tensor given by

$$\hat{\mathbf{R}}(\mathbf{X}, t) = \mathrm{Div}\mathbf{P} + \mathbf{B}, \tag{50}$$

$$\boldsymbol{\tau}_{\Omega}(\mathbf{X}, t) = \left(b_{\Omega}^e \int_{\Omega_e} b_{\Omega}^e \, \mathrm{d}\Omega\right) \mathbf{D}^{-1}, \tag{51}$$

$$D_{ij} = \int_{\Omega_e} \frac{\partial b_{\Omega}^e}{\partial X_k} S_{kp} \frac{\partial b_{\Omega}^e}{\partial X_p} \delta_{ij} \, \mathrm{d}\Omega + \int_{\Omega_e} \frac{1}{4} \left[F_{ip} \frac{\partial b_{\Omega}^e}{\partial X_q} + \frac{\partial b_{\Omega}^e}{\partial X_p} F_{iq}\right] C_{pqkl} \left[F_{jk} \frac{\partial b_{\Omega}^e}{\partial X_l} + \frac{\partial b_{\Omega}^e}{\partial X_k} F_{jl}\right] \mathrm{d}\Omega. \tag{52}$$

Remark 5. Since the stabilized form (46) is completely expressed in terms of the coarse-scale fields, therefore, to keep the presentation simple, we have reverted to the notation without "hats" in (46).

3.3. Stabilized finite element formulation

We now consider a partition of the domain Ω_0 into open non-overlapping finite elements subdomains $\{\Omega^e\}_{e=1}^{n_{el}}$ where n_{el} is the total number of elements such that $\overline{\Omega} = \cup_{e=1}^{n_{el}} \overline{\Omega}^e$. The semi-discrete weak form is: Find $(\boldsymbol{\varphi}^h, \Theta^h) \in \mathcal{S}^h \times \mathcal{Q}^h$ such that $\forall (\boldsymbol{\eta}^h, w^h) \in \mathcal{V}^h \times \mathcal{P}^h$,

$$\begin{cases} R_{\boldsymbol{\varphi}}^{\text{stab}}(\boldsymbol{\eta}^h, \boldsymbol{\varphi}^h, \Theta^h, \gamma, \mathbf{E}^i) = 0, \\ R_{\Theta}(w^h, \boldsymbol{\varphi}^h, \Theta^h, \gamma, \mathbf{E}^i) = 0, \end{cases} \tag{53}$$

where γ is defined by (36), $\mathbf{E}^i$ is defined by (32), and the discrete function spaces are defined as follows.

$$\begin{aligned} \mathcal{S}^h &= \{\boldsymbol{\varphi} \in \mathcal{S} : \boldsymbol{\varphi}(\mathbf{X}, t) \in \mathcal{Y}_k\}, & \mathcal{V}^h &= \{\boldsymbol{\eta} \in \mathcal{V} : \boldsymbol{\eta}(\mathbf{X}) \in \mathcal{Y}_k\}, \\ \mathcal{Q}^h &= \{\Theta \in \mathcal{Q} : \Theta(\mathbf{X}, t) \in \mathcal{Y}_k\}, & \mathcal{P}^h &= \{w \in \mathcal{P} : w(\mathbf{X}) \in \mathcal{Y}_k\}, \end{aligned} \tag{54}$$

where $\mathcal{Y}_k = C^0(\Omega_0) \cap P_k(\Omega^e)$ is the space of piecewise continuous polynomial functions and $\mathcal{S}^h, \mathcal{V}^h, \mathcal{Q}^h$, and $\mathcal{P}^h$ are closed linear subspaces of $\mathcal{S}, \mathcal{V}, \mathcal{Q}$, and $\mathcal{P}$ respectively.

The stabilized system of equations in (53) leads to a fully coupled mixed-field problem that is amenable to consistent linearization. One attribute of stabilized methods is that they allow the use of arbitrary combination of interpolation functions for the displacement and temperature fields. A significant outcome of this relaxation is that all the stability parameters can be variationally derived, and that they are free of any user-defined parameters. These features of the method are exploited to develop a monolithic solution algorithm where all unknown fields are solved concurrently. Together with consistent linearization of the monolithic variational form, this algorithm leads to higher convergence of the solution in the Newton–Raphson method.

Remark 6. Numerical investigation of the stability tensor in (51) shows that it adapts with the spatio-temporally varying solution fields. This self-adjusting feature of the stability tensor helps with optimal convergence of the residual-based error in the variational form. Since the complexity of the physical phenomenon varies as a function of space and time as the polymerization front traverses the domain, this aspect of the formulation is of unique significance in the application of the method to problems of FP.

Remark 7. In this work we have used the same order of polynomials for $\boldsymbol{\varphi}^h$ and Θ^h. This results in an easy to implement numerical method.

3.4. Time integration schemes

Expanding $\boldsymbol{\varphi}$ and Θ in terms of finite element shape functions and substituting the expansion in (53) results in a coupled system of nonlinear ordinary differential equations. To solve the initial value problem, we consider a partition of the time interval under consideration $[0, T]$ into discrete time intervals where we define $t_n \in \{0 = t_0, t_1, \ldots, t_{L-1}, t_L = T\}$. Let subscript n denote functions evaluated at time t_n, for example, $\boldsymbol{\varphi}_n(\mathbf{X}) = \boldsymbol{\varphi}(\mathbf{X}, t_n)$. We denote current time step as t_{n+1} and the previous time step as t_n. Since the time scales for cure evolution, inelastic strain evolution, and heat propagation can vary considerably, we use a combination of ODE solvers in (53) for computational efficiency. Finally, the Newton–Raphson method is used to solve the resulting system of nonlinear algebraic equations wherein the following steps are taken at each Newton iteration:

- *Step 1:* At each integration points, solve the curing model (36) for γ_{n+1}. Discussion on ODE solver that is employed to solve (36) is given in Section 4.1.
- *Step 2:* At each integration points, solve the flow rule (37) for $\mathbf{E}^i_{n+1}$. Exploiting the fact that (27) is invertible, the flow rule can be solved analytically by enforcing (30) as follows.

$$\mathbf{E}^i_{n+1} = \mathbf{E}_n - \left(\frac{\lambda(\gamma_{n+1})}{2\mu(\gamma_{n+1})(3\lambda(\gamma_{n+1}) + 2\mu(\gamma_{n+1}))} (\text{tr } \mathbf{S}_n)\mathbf{I} + \frac{1}{2\mu(\gamma_{n+1})} \mathbf{S}_n + \alpha \mathbf{I}(\Theta_n - \Theta_{\text{ref}}) \right). \tag{55}$$

- *Step 3:* Apply any appropriate ODE solver (where it can be different from that used in Step 1) to (53) to obtain a system of nonlinear algebraic equations. In this paper, we employ the implicit midpoint method which is an A-stable and second-order accurate ODE solver.

A summary of the solution procedure is presented in Box II.

4. Numerical examples

Materials that can sustain frontal polymerization need to have certain chemical and thermal properties, namely, they need to be (i) thermally initiating where they undergo a rapid exothermic chemical reaction when heated to initiate polymerization, (ii) possess low heat dissipation property that helps sustain the exothermic reaction as it propagates, (iii) have a relatively low activation energy to facilitate initiation under controlled conditions, and (iv) possess good thermal insulation properties that can help retain the heat generated during polymerization, thereby promoting the self-sustaining reaction front. Certain acrylate monomers and mixtures, and some epoxy resins have been investigated for FP (Pojman, 2012) due to their reactivity and ability to propagate the polymerization reaction in a self-sustained manner. Likewise, thermosetting polymers, where reaction leads to the formation of three-dimensional networks, providing enhanced mechanical properties, have also been employed in FP.

1. Initial conditions at t_n: Data structure
   i. Initial conditions for internal variables at quadrature points $\{\gamma_n, \mathbf{E}^i_n\}$
   ii. Initial conditions for finite element solution fields at nodal points $\{\boldsymbol{\varphi}^h_n, \Theta^h_n\}$
2. Let $\{\boldsymbol{\varphi}^{h,k}_{n+1}, \Theta^{h,k}_{n+1}, \gamma^k_{n+1}, \mathbf{E}^{i,k}_{n+1}\}$ be the solutions at the k-iteration of Newton–Raphson procedure. Use finite element interpolation to compute $\{\boldsymbol{\varphi}^h_n, \Theta^h_n\}$ and $\{\boldsymbol{\varphi}^{h,k}_{n+1}, \Theta^{h,k}_{n+1}\}$ at quadrature points.
3. Update the internal variables
   i. Compute γ^k_{n+1} from (36)
   ii. Compute $\mathbf{E}^{i,k}_{n+1}$ from (55)
4. Compute the first Piola–Kirchhoff Stress tensor $\mathbf{P}(\mathbf{E}^{h,k}_{n+1}, \mathbf{E}^{i,k}_{n+1}, \Theta^{h,k}_{n+1}, \gamma^k_{n+1})$
5. Compute the heat flux vector $\mathbf{Q}(\mathbf{E}^{h,k}_{n+1}, \mathbf{E}^{i,k}_{n+1}, \Theta^{h,k}_{n+1}, \gamma^k_{n+1})$
6. Compute residual at the k-iteration

$$\mathbf{R}^k_{n+1} \equiv \begin{bmatrix} R^{\text{stab}}_{\boldsymbol{\varphi}}(\boldsymbol{\eta}^h, \boldsymbol{\varphi}^{h,k}_{n+1}, \Theta^{h,k}_{n+1} h, \gamma^k_{n+1}, \mathbf{E}^{i,k}_{n+1}) \\ R_\Theta(\boldsymbol{\eta}^h, \boldsymbol{\varphi}^{h,k}_{n+1}, \Theta^{h,k}_{n+1} h, \gamma^k_{n+1}, \mathbf{E}^{i,k}_{n+1}) \end{bmatrix}$$

7. Let ε_{NR} be the convergence criterion for the Newton–Raphson iteration. IF $\|\mathbf{R}^k_{n+1}\| > \varepsilon_{\text{NR}}$ THEN: Continue iteration

   Compute tangent matrix

$$\mathbf{K}^k_{n+1} = \left[\begin{array}{c|c} \partial R^{\text{stab}}_{\boldsymbol{\varphi}} / \partial \boldsymbol{\varphi}^{h,k}_{n+1} & \partial R^{\text{stab}}_{\boldsymbol{\varphi}} / \partial \Theta^{h,k}_{n+1} \\ \hline \partial R_\Theta / \partial \boldsymbol{\varphi}^{h,k}_{n+1} & \partial R_\Theta / \partial \Theta^{h,k}_{n+1} \end{array}\right]$$

   Update $[\boldsymbol{\varphi}^{k+1}_{n+1}, \Theta^{k+1}_{n+1}]^T = [\boldsymbol{\varphi}^k_{n+1}, \Theta^k_{n+1}]^T - [\mathbf{K}^k_{n+1}]^{-1} \mathbf{R}^k_{n+1}$

   Set $k = k + 1$ and GO TO STEP 2

   ELSE: Update data structure

   Internal variables at quadrature points $\{\gamma_{n+1}, \mathbf{E}^i_{n+1}\} = \{\gamma^k_{n+1}, \mathbf{E}^{i,k}_{n+1}\}$

   Finite element solution fields at nodal points $\{\boldsymbol{\varphi}^h_{n+1}, \Theta^h_{n+1}\} = \{\boldsymbol{\varphi}^{h,k}_{n+1}, \Theta^{h,k}_{n+1}\}$

   END IF

Box II. Monolithic solution algorithm.

From the materials perspective an important aspect of polymer chemistry in FP is the reaction kinetics that governs the polymerization process. The rate at which monomers are converted into polymers directly influences the self-sustaining nature of the reaction front and the overall dynamics of the process. Controlling reaction kinetics involves considerations of activation energy that is required to initiate the polymerization reaction, as lower activation energy often leads to faster reaction rates. Furthermore, temperature control is crucial for maintaining a stable and controlled reaction front.

In this paper, we consider FP of dicyclopentadiene (DCPD). The curing model and corresponding parameters are taken from Kumar et al. (2024). The evolution equation for the degree of cure γ is given as follows.

$$\dot{\gamma} = A_\gamma \exp\left(\frac{-E_\gamma}{RT}\right)(1-\gamma)^n \gamma^m \frac{1}{1+\exp(C_d(\gamma-\gamma_d))}, \tag{56}$$

where A_γ (in 1/s) is the time constant, E_γ (in J/mol) is the activation energy, R (8.314 J/(mol K)) is the universal gas constant, n, m are parameters defining the order of reaction in Prout–Tompkins model, and C_d, γ_d are parameters that describe the diffusion-controlled reaction kinetics at high value of γ. The mechanical material parameters are then defined as follows.

$$E(\gamma) = E_2 + \frac{E_1 - E_2}{1+\exp(C_E(\gamma-\gamma_E))}, \tag{57}$$

$$\nu(\gamma) = \nu_2 + \frac{\nu_1 - \nu_2}{1+\exp(C_\nu(\gamma-\gamma_\nu))}, \tag{58}$$

Table 1
Elastic parameters for dicyclopentadiene (DCPD).

$E_1 = 0.3$ kPa	$E_2 = 2100$ MPa	$C_E = 25$	$\gamma_E = 0.89$
$\nu_1 = 0.48$ kPa	$\nu_2 = 0.416$ MPa	$C_\nu = 11.92$	$\gamma_\nu = 0.70$

Table 2
Cure kinetic and thermal parameters for dicyclopentadiene (DCPD).

$A_\gamma = 8.55 \times 10^{15}$ 1/s	$E_\gamma = 110,750$ J/mol	$n = 1.77$	
$m = 0.81$	$C_d = 14.41$	$\gamma_d = 0.41$	
$C_\Theta = 1600$ J/kgK	$\rho_0 = 980$ kg/m^3	$k = 0.15$ W/mK	$\alpha = 10^{-4}$ K^{-1}

$$\kappa(\gamma) = \frac{E(\gamma)}{3(1 - 2\nu(\gamma))}, \tag{59}$$

$$\mu(\gamma) = \frac{E(\gamma)}{2(1 + \nu(\gamma))}, \tag{60}$$

where E_1, ν_1 and E_2, ν_2 are elastic modulus and Poisson's ratio at $\gamma = 0.1$ and $\gamma = 1$, respectively, while $C_E, C_\nu, \gamma_E, \gamma_\nu$ are the fitting parameters. The value of the parameters for DCPD are listed in Tables 1 and 2. The heat released from the exothermic reaction is $C_\gamma = \rho_0 H_R$ where $H_R = 3.5 \times 10^5$ J/kg. It is important to note that the elastic modulus increases by several orders of magnitude within a narrow range of the degree of cure γ from 0.7 to 0.9. Likewise, the Poisson's ratio changes from nearly incompressible to slightly compressible with a change in γ from 0.5 to 0.9. The reaction front between the cured and uncured parts of the material leads to rapid change in the mechanical material properties as a function the degree of cure. This traveling reaction front also results in embedding local deformations in the continuously evolving microstructure of the printed material as shown in the numerical test cases presented below.

A goal of this section is to demonstrate the applicability of the formulation presented in Section 3 to coupled thermo–chemo–mechanical problems in FP. These test problems showcase different aspects of the formulation, namely, finite strains, coupled physical response, frozen inelastic deformation as the material cures, as well as algorithmic aspects of the monolithic solution scheme. The method is implemented using linear hexahedral elements for all the degrees of freedom, and a 3×3 Gauss quadrature rule is used for numerical integration. The curing kinetics coefficient for the degree of cure γ is obtained by numerically solving the corresponding ODEs at the integration points. At each time step, the stabilized weak form of the nonlinear mixed-field problem is monolithically solved via the Newton–Raphson method with consistently linearized tangent matrix that leads to faster convergence. Generalized minimal residual (GMRES) method with Additive Schwarz method (ASM) preconditioner is used to solve the system of linear equations.

4.1. ODE solvers for the curing model

The curing model is an essential component of the FP model as it is directly related to the release of energy that is crucial for self sustaining the propagaition of the polymerization front across which the evolution of mechanical and thermal properties of the material take place. The accuracy of the numerical solution of the curing model greatly affects the computed physics, namely, the speed of the reaction front, local strains that get trapped in the morphology of the material due to the formation of new bonds, and formation of curing induced residual stresses. For materials of practical interest in FP, such as the material parameters given in Table 2, accurately resolving the curing model necessitates using much smaller time step size as compared to the time step size needed to solve the balance of energy equation. Therefore, computational expediency suggests using different ODE solvers for the curing model and the balance of energy equation, and that is the line of thought adopted here.

In this section, we investigate several ODE solvers for the curing model presented in Eq. (36). ODE solvers listed in Table 3 are employed with initial condition $\gamma_0 = 0.1$ and temperature $\Theta = 230$ °C, as were used in the experimental studies to trigger FP polymerization in DCPD reported in Kumar et al. (2024). The numerically computed value of γ for various time step sizes, and of the reduction in the relative error as a function of time step for the various ODE integrators is shown in Fig. 1 where the solution from `Lob6` with time step $\Delta t = 10^{-8}$ s is used as the reference γ^{ref} value to compute the error. The error of first-order methods, i.e., `FE` and `BE`, are quite large while the explicit methods, namely, `FE` and `Law5` have severe limitation on the permissible time step size Δt. These explicit methods fail to yield solution for larger time step sizes than the one presented in Fig. 1. Among the other methods, `Rad5` and `Lob6` give good numerical solution even with relatively large Δt. In the subsequent sections, `Rad5` with time step size of the order of 10^{-3} s is used for the various numerical test cases.

4.2. Frontal polymerization in 1D specimen subjected to oscillatory loading

To verify the proposed numerical method, we consider a 1D problem (Kumar et al., 2022) where a bar of length L is fixed at $X = 0$ and subjected to a Dirichlet boundary condition $\eta(t) = A(1 - \cos(\omega t))$ at $X = L$. At time $t = 0$, temperature induced polymerization is initiated at $X = 0$. Let X_f be the coordinate of the reaction front and $E_1 = E(\gamma_0)$, $E_2 = E(1)$ be the elastic moduli at the initial and the maximum degree of cure, respectively. The analytical solution is derived under the assumptions of small deformation, $\mathbf{F} \to \mathbf{I}$, with no heat loss to the environment, and with coefficient of thermal expansion $\alpha = 0$. The front propagates at a steady speed V_f. The thermal and reaction fronts coincide at X_f and are mathematically sharp. In addition, the temperature field and curing parameter are assumed to have the following values with respect to the location of the reaction front X_f:

Table 3
ODE solvers.

Name	Solver	Type	Order	A-stable	Reference
FE	Forward Euler	explicit	1	✗	–
Law5	Lawson's RK5	explicit	5	✗	Lawson (1966)
Ros4	Rosenbrock 4P2	linearly implicit	4	✓	Steinebach (2020)
BE	Backward Euler	implicit	1	✓	–
Rad5	Radau IA	implicit	5	✓	Ehle (1969)
Lob6	Lobatto IIIC	implicit	6	✓	Chipman (1971)

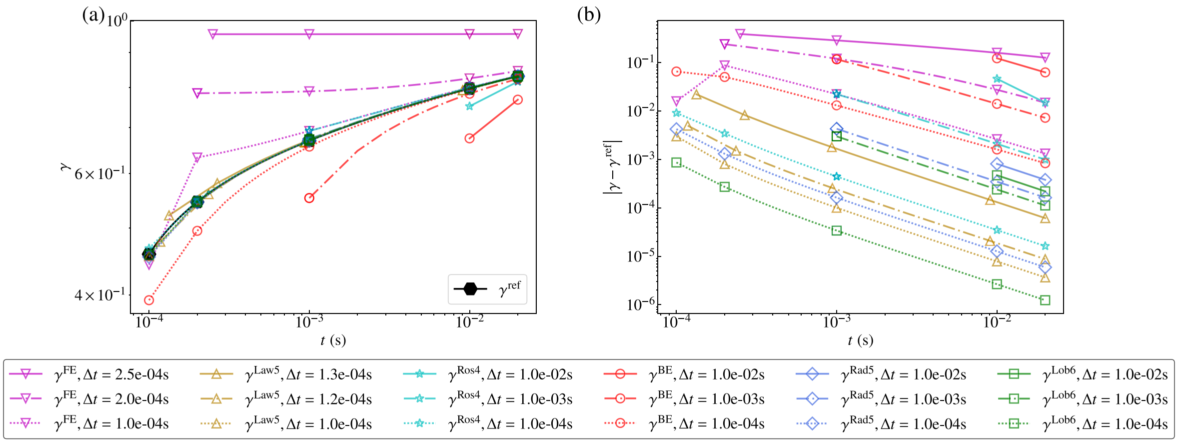

Fig. 1. Comparison between ODE solvers: (a) numerical solutions; (b) error in the numerical solutions.

(i) for $X > X_f$: $\Theta = \Theta_0$ and $\gamma = \gamma_0$,
(ii) for $X < X_f$: $\Theta = \Theta_{max} = T_0 + (1 - \gamma_0)H_r/C_\Theta$ and $\gamma = 1$.

Likewise, the value of the modulus of elasticity in the regions that are split by the reaction front is given as:

(i) $E = E_1$ for $X \in [X_f, 1]$ and $E = E_2$ for $X \in [0, X_f]$,
(ii) $E_1 \ll E_2$ such that $E_1/E_2 \approx 0$.

Let $\bar{X} = X/L$, $\bar{u} = u/A$, and $\bar{t} = V_f t/L$. Following Kumar et al. (2022) and under the assumption that $\alpha = 0$ and $E_1 \ll E_2$, the analytical solution for a given (but otherwise arbitrary) front propagation speed V_f is

$$\bar{u}(\bar{X}, \bar{t}) = \begin{cases} \frac{1}{A}\int_0^{\bar{X}} \varepsilon(y)\,\mathrm{d}y & \text{if} \quad \bar{X} \in [0, X_f/L] \\ 1 - \cos\left(\omega\bar{t}\right) - \frac{1}{A}\varepsilon\left(\bar{t}\right)\left(1 - \bar{X}\right) & \text{if} \quad \bar{X} \in [X_f/L, 1] \end{cases} \tag{61}$$

where

$$\varepsilon(\bar{t}) = A\omega\left(\sin(\omega)\mathrm{Ci}(\omega) - \cos(\omega)\mathrm{Si}(\omega) - \sin(\omega)\mathrm{Ci}\left(\omega - \omega\bar{t}\right) + \cos(\omega)\mathrm{Si}\left(\omega - \omega\bar{t}\right)\right), \tag{62}$$

$$\mathrm{Si}(x) = \int_0^x \frac{\sin t}{t}\,\mathrm{d}t, \qquad \mathrm{Ci}(x) = \int_x^\infty \frac{\cos t}{t}\,\mathrm{d}t. \tag{63}$$

To solve the problem, we consider dimension of the bar as length $L = 5\,\mathrm{mm}$, and a uniform square cross-section with side length $s = 0.5\,\mathrm{mm}$. We apply fixed boundary condition at $X = 0$, and $u^D = \eta$ at $X = L$, where $A = 0.01\,\mathrm{mm}$ and $\omega = 0.1\,\mathrm{s}^{-1}$. To trigger the polymerization process, a temperature trigger $T_{\mathrm{trig}} = 230\,°\mathrm{C}$ is applied at $X = 0$. The spatial domain is discretized with a uniform mesh comprised of 1000 linear hexahedral elements in the longitudinal direction A uniform time step size $\Delta t = 0.001\,\mathrm{s}$ is used. The numerically-obtained average front speed is found to be $V_f = 1.18\,\mathrm{mm/s}$ and is subsequently used to compute the analytical solution to the problem. Fig. 2(a) shows the comparison between spatial distribution of the numerically computed displacement field and the analytical solution. Fig. 2(b) shows the evolution of temperature profile wherein steep temperature gradients mark the locations of the curing front for different points in time during the evolution of the problem. Fig. 3 shows the degree of cure and inleastic stain respectively at time $\tilde{t} = 0.75$.

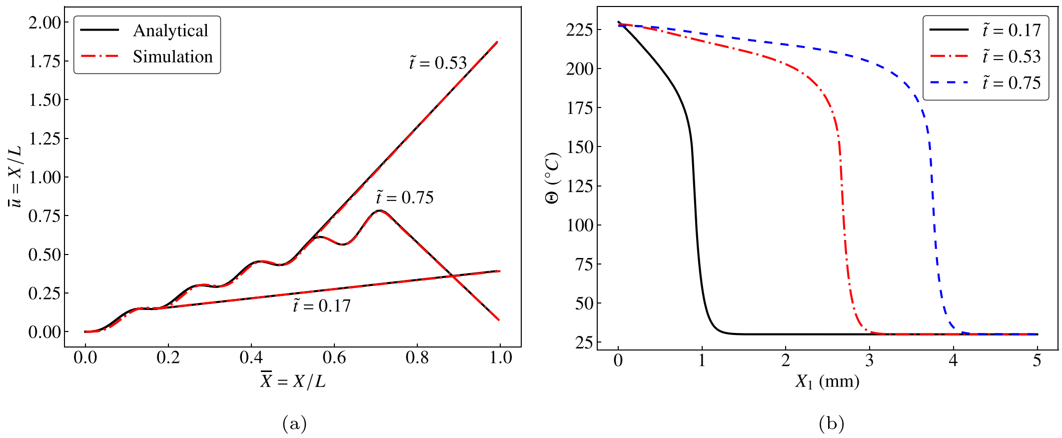

Fig. 2. Verification of the numerical method given in Section 3: (a) comparison of the numerical prediction of the displacement field with analytical solution; (b) evolution of temperature profile.

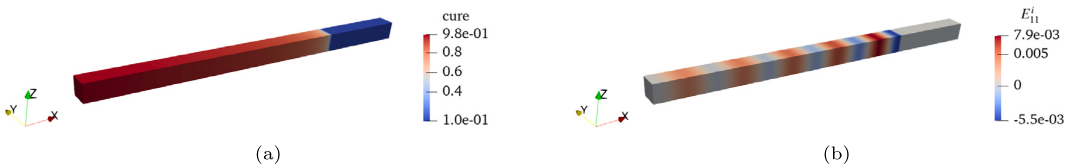

Fig. 3. Simulation results at $\tilde{t} = 0.75$: (a) degree of cure γ; (b) inelastic strain, E^i_{11}.

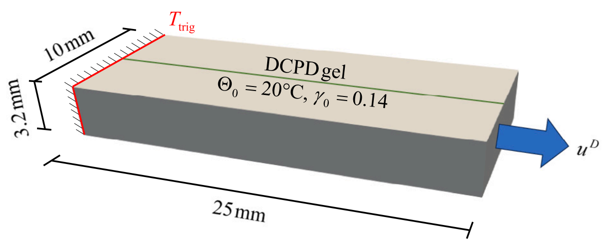

Fig. 4. Problem description: dimension and boundary conditions.

4.3. Frontal polymerization in 3D block subjected to periodic loading

This section presents validation of the model and the numerical method by comparing simulations with experimental data. We consider a 3D block made of DCPD as shown in Fig. 4. One edge of the block is fixed, and the opposite edge is subjected to a periodic displacement field $u^D = 0.01(1 - \cos(2\pi t))$ in the longitudinal direction. To initiate the polymerization process, trigger temperature $T_{\text{trig}} = 210$ °C is applied at the fixed end. It is assumed that there is no heat loss to the environment, and therefore, zero Neumann boundary condition is applied on all other sides. The spatial mesh is comprised of $5000 \times 10 \times 4$ linear hexahedral elements.

We first investigate the effect of time step size on the accuracy of the computed solution. Fig. 5 shows the comparison between two simulations using uniform time step $\Delta t = 0.005$ s and $\Delta t = 0.001$ s. The plot shows the relative z-displacement along the centerline of the bottom surface of the plate. Since the difference between these two computed results is relatively small, $\Delta t = 0.005$ s is used for the rest of the simulations in this section. The comparison between the present model and the experimental data from Kumar et al. (2022) for five cycles is shown in Fig. 6. Cyclic loading combined with FP results in freezing of the inelastic deformation that appears as the repeated displacement pattern on the surface of the block as shown in Fig. 7. In addition to the mechanical deformation that arises in response to the applied loading, this pattern is a product of two important physical mechanisms: (i) traveling curing front (Fig. 7(a)) in FP, and (ii) energy dissipating inelastic processes (Fig. 7(b)) in material evolution. The former is captured by the transient heat equation and the curing model, while the later is captured by the evolution Eq. (32).

Next, we investigate the effect of heat loss to the environment by replacing zero Neumann boundary conditions, as in the previous simulation, with the Robin boundary conditions. The ambient temperature is $\Theta_\infty = \Theta_0 = 20$ °C and the heat transfer coefficient is assumed to be $H_\Theta = 15\,\text{W/m}^2$ °C. Heat loss to the environment results in less energy in the system to sustain the process of

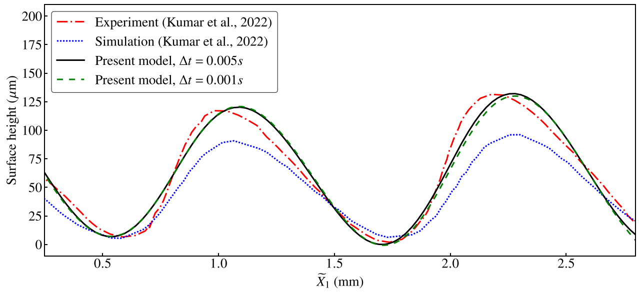

Fig. 5. Study of the accuracy of the solution with uniform time step $\Delta t = 0.005$ and $\Delta t = 0.001$.

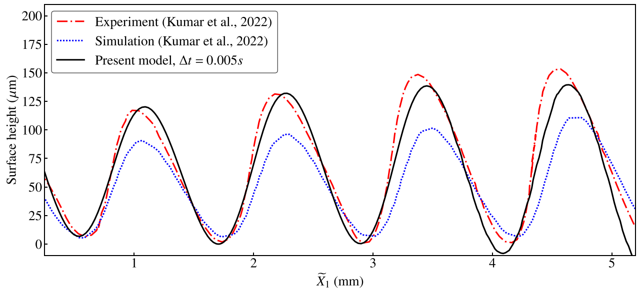

Fig. 6. Comparison between computed results and experimental data for five loading cycles.

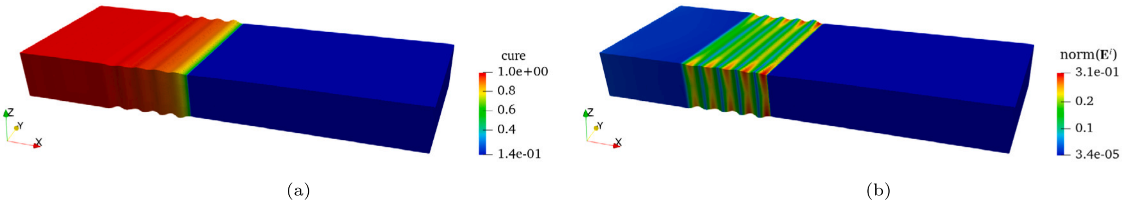

Fig. 7. Simulation results: (a) degree of cure γ; (b) norm of the inelastic strain $\mathbf{E}^i$.

polymerization which can also slow down the speed of propagation of the front. The model predicts the front speed of 0.602 mm/s and 0.573 mm/s for the cases where heat loss is ignored, and the one where heat loss is accounted for via Robin boundary conditions, respectively. The front speed also affects the resulting deformation pattern as shown in Fig. 8. The evolution of material parameters, temperature profile, and the inelastic strains are shown in Fig. 9. As the curing front traverses through the material body which is simultaneously being subjected to oscillatory displacement boundary condition, large local strains that are caused by tensile loading, but not released because of the curing induced formation of new bonds, lock the deformation locally into the morphology of the material. Fig. 9(a) shows profiles of two mechanical materials properties, elastic modulus and Poisson's ratio that are shown on the deformed shape of the curing material. Likewise, Fig. 9(b) shows the norm of the strain tensor, and isosurfaces of the temperature field where thermal loss to the ambient environment can clearly be seen. Fig. 10 presents the evolution of elastic modulus, Poisson's ratio, temperature, and the norm of the inelastic strain, plotted along the centerline of the top surface of the block as shown with the green line in Fig. 4. Note that the elastic modulus ahead of the front shown in Fig. 10(a) is not zero, but it is several orders of magnitude smaller as compared to the elastic modulus of the curing material behind the front.

Table 4 shows the convergence of the residual in the Newton–Raphson loops at various points in time during the evolution of the problem. As described in Section 3.3, the stabilized mixed-form that allows using equal order interpolations for the various fields also lends itself to consistent linearization that results in rapid convergence of the solution even in the presence of complex evolving physics.

4.4. Frontal polymerization in the printing of coil structure via extrusion-based direct ink writing (DIW)

This section demonstrates the applicability of the proposed material model to FP-DIW manufacturing process. It is an example of an open system thermodynamic problem where mass (material) is continuously being injected in the system. The algorithm that simulates material deposition in DIW is based on Wijaya et al. (2022) where printing process is modeled via activation of

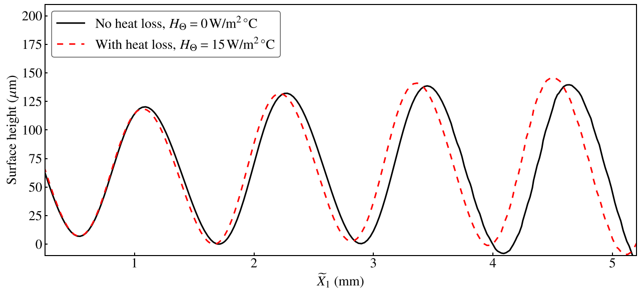

Fig. 8. Surface patterns with and without heat loss to the environment.

Table 4
Convergence of the Newton–Raphson method.

Iter	Step 100	Step 1000	Step 2000	Step 3000
0	9.00625e+00	1.09184e+01	1.39182e+01	1.79384e+01
1	9.17452e−02	1.20023e−01	1.39122e−01	4.55740e−01
2	1.45198e−04	2.31998e−04	5.12602e−03	1.18152e−02
3	3.82324e−06	3.93655e−06	6.70904e−04	1.60381e−03
4			7.67629e−05	1.71222e−04
5			1.37690e−05	3.24312e−05
6				3.89795e−06

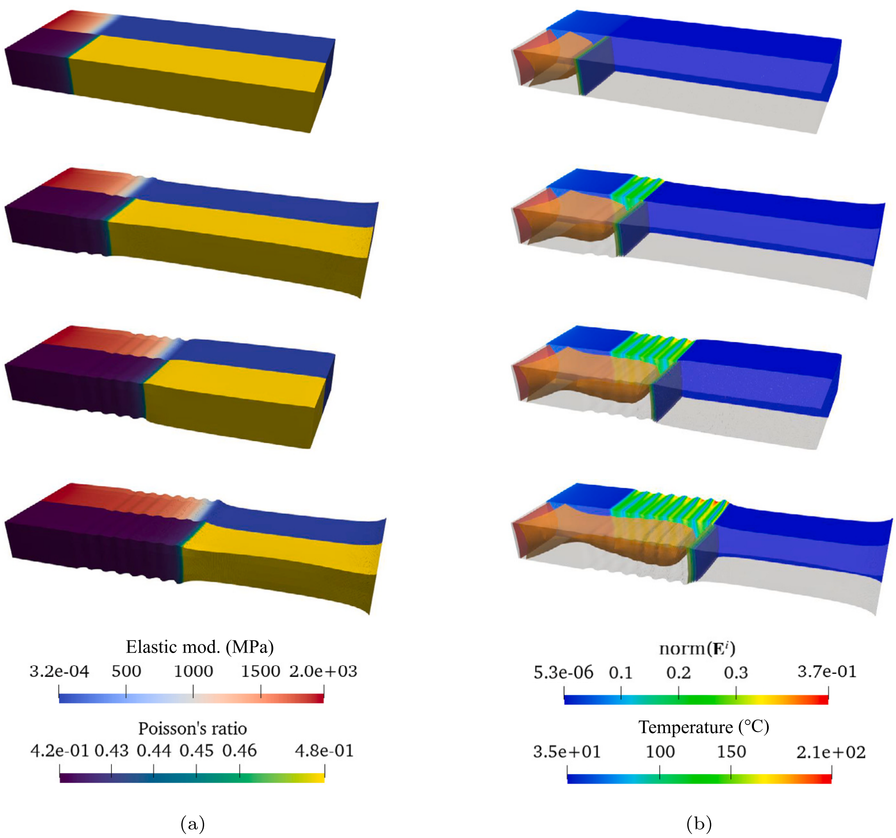

Fig. 9. Deformed configuration at four time points for the DCPD gel specimen subjected to cyclic loading: (a) evolution of elastic modulus and Poisson's ratio; (b) temperature and norm of elastic strain (shown on the deformed configuration).

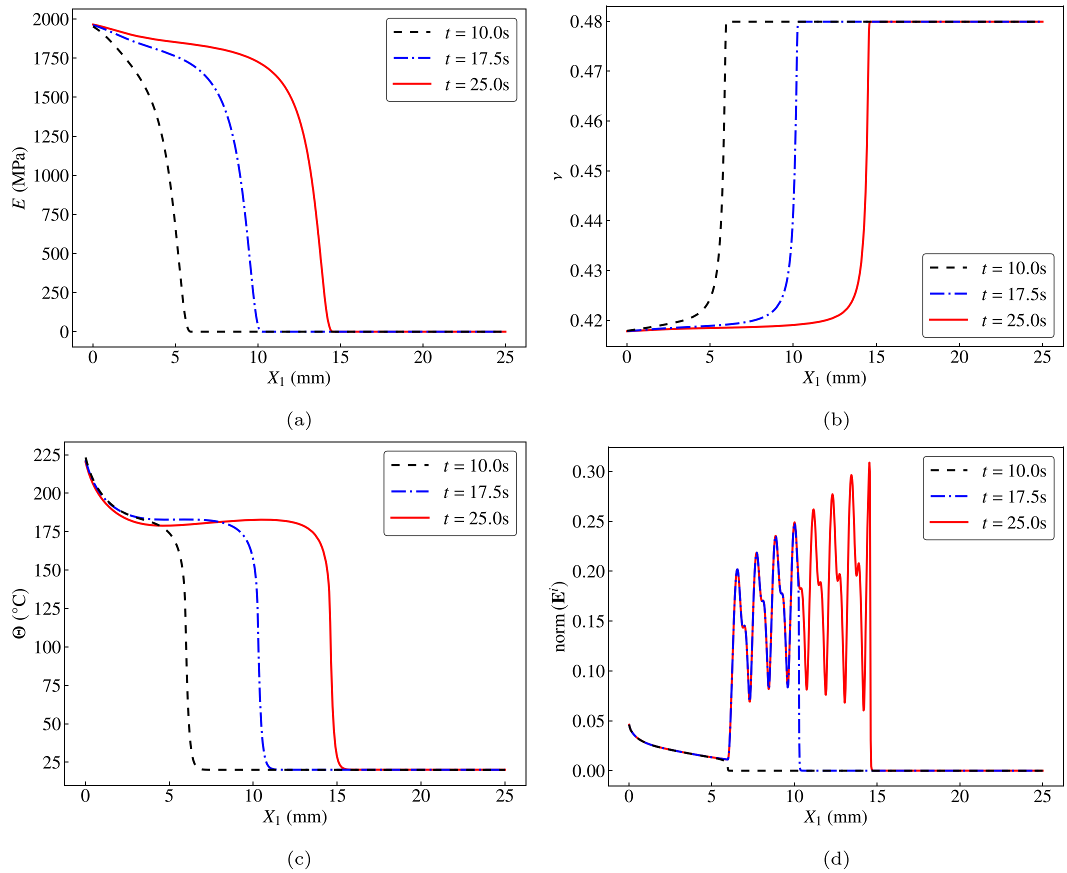

Fig. 10. Evolution of quantities along the centerline of the plate's top surface: (a) elastic modulus; (b) Poisson's ratio; (c) temperature; and (d) norm of the inelastic strain.

the material parameters in the elements that are currently being printed. Once activated in an element, these parameters keep track of the evolution of material properties as that element now belongs to the printed material zone in the mesh. This ghost mesh method bypasses the need to keep creating new segments of the mesh around the current location of the moving printing nozzle. The algorithm employs a binary internal variable $\phi = \{0, 1\}$ at every material point that identifies whether the material has been printed at that point or not. We set $\phi = 1$ if the material has been printed, and set $\phi = 0$ otherwise. Then, a moving point $\mathbf{p}(t) = (X_1^p(t), X_2^p(t), X_3^p(t))$ and a printing region $\mathcal{R}_\mathbf{p}$ around point $\mathbf{p}$ are defined to represent the current position of the printing nozzle and the region where material is being deposited, respectively. At the start of the process, we set $\phi = 0$ at all the material points. Subsequently, in any generic time step, we set $\phi = 1$ at all points that reside inside $\mathcal{R}_\mathbf{p}$. Some examples of how to define $\mathbf{p}$ and $\mathcal{R}_\mathbf{p}$ can be found in Wijaya et al. (2022).

To minimize the effect of the ghost mesh (i.e., part of the mesh where material has not yet been deposited), the material parameters are scaled to a low value as follows: In an element where $\phi = 0$, $E(\gamma)$ is scaled by a parameter, chosen to be an arbitrary small positive number $\epsilon_E > 0$, while the body force is set as $\mathbf{B} = \mathbf{0}$. This modification ensures that the region where the material has not yet been deposited does not contribute to mechanical loading caused by self-weight, and it also has negligible contribution to the stiffness of the ghost part of the mesh. It is observed that the material ejected from the nozzle in the form of a highly viscous fluid has some local tensile capacity that counteracts the self weight of this small segment of material as it rests at the tip of the coil. To account for this tensile effect, which counters the self weight of this small segment, the density of the newly ejected material is scaled as a function of time elapsed since the ejection of the material from the nozzle. In the region where the material is already deposited ($\phi = 1$), the body force is set equal to

$$\mathbf{B} = \begin{bmatrix} 0 \\ 0 \\ g C_\rho \rho_0 \end{bmatrix}, \tag{64}$$

where g is acceleration due to gravity, and C_ρ is a scale factor for the self-weight given by

$$C_\rho = \frac{1}{1 + \exp\left(-10\left(t_{n+1} - t_p - 0.5\right)\right)}, \tag{65}$$

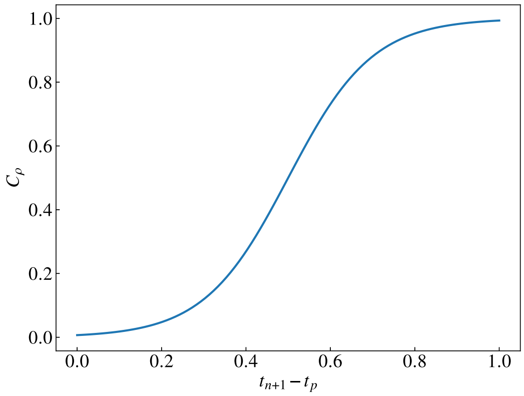

Fig. 11. Scaling factor for self-weight in FP-DIW.

and t_p is the time when the material is deposited. Each material point associated with the corresponding integration point in the mesh has its associated t_p which is the time when the binary internal variable ϕ switches from 0 to 1. The plot of scale factor for adjusting the self weight is given in Fig. 11. Note that $E(\gamma)$ which evolves as a function of cure is not multiplied by the scaling parameter.

Remark 8. In the interest of simplicity, we have not accounted for the swelling of the material as it exits the printing nozzle. For models that can capture these features, intended reader is referred to Kumar et al. (2024) and Zakoworotny et al. (2024).

The material model in Box 1 and the printing algorithm described above are combined and solved using the monolithic solution algorithm in Box 2 to simulate the direct ink writing of the coil structure. The radius of the coil is 2 mm and the radius of the filament is 0.75 mm. The speed of the nozzle is adjusted such that the cure at the top of the print front is $\gamma = 0.3$. In other words, the print speed automatically adapts to the rate of cure with a given threshold, and is not a predefined value. The process of material deposition is shown in Fig. 12. Fig. 12(a) shows the curing front, which follows the material injection front, with rapid curing occurring in the region around the leading tip. The increase in the modulus of elasticity as a function of time is shown in Fig. 12(b). It is important to note that the force of gravity that is always acting on the material as it gets deposited and cures, results in deformation and associated stresses that are shown in Fig. 12(c). Fig. 13 shows the vertical deformation of the centerline of the coil, thereby highlighting the deviation of the printed object from that of the intended geometric shape in Fig. 13-b.

Remark 9. Experimental studies show that material expands when extruded from the nozzle. This expansion can be accounted for by applying pre-stress to the newly extruded material as discussed in Kumar et al. (2024).

5. Conclusion

We have presented a coupled thermo–chemo–mechanical model for frontal polymerization in which a self-propagating reaction front moves through the material, converting monomers into polymers. The propagation is supported by exothermic reaction of monomers which releases heat as the process of polymerization progresses. This heat propagates through the material via diffusion and triggers an exothermic reaction in the material. A constitutive model that accounts for heat generation, heat transfer, and reaction kinetics is presented to simulate polymerization, and predict the rate at which the monomers are converted into polymers with the associated heat release. We show that the second law of thermodynamics implies the existence of an inelastic process that is associated with curing induced material evolution. An evolution equation for inelastic strains that satisfies the second law is proposed.

A residual-based stabilized finite element formulation is employed that constitutes the basis of the numerical method. A unique feature of VMS-based stabilization is the notion of hierarchical modeling of fine-scale physics that may otherwise be beyond the resolution capacity of the computational grid. These fine-scale closure models are functions of the residuals of the Euler–Lagrange equations of the global model. Embedding the closure models back in the variational formulation enhances the stability of the method as well as the accuracy of the numerical scheme. The stabilized nonlinear coupled-field formulation successfully accommodates equal order interpolation functions for the displacement and temperature fields. This mathematical attribute helps in consistent linearization of the formulation to develop a monolithic algorithm where all the fields are concurrently solved. In addition, variational coupling of the mechanical and thermal fields together with consistently linearized tangent matrix helps in achieving faster convergence of the solution in the Newton–Raphson iterations for the investigated test cases. Due to the difference in the time scales of cure evolution, inelastic strain evolution, and the rate of heat propagation, we have employed a combination of ODE solvers to solve the corresponding evolution equations in a computationally efficient manner.

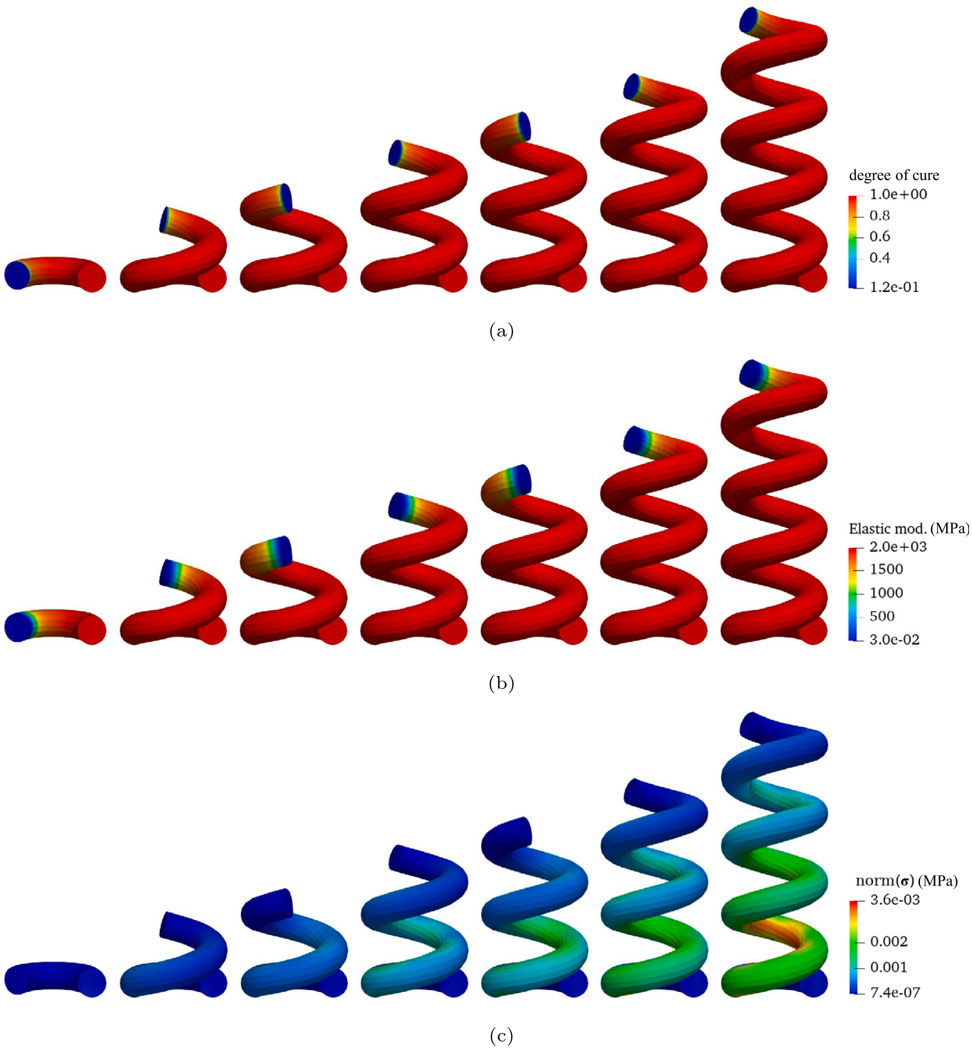

Fig. 12. Printing of coil structure via extrusion-based direct ink writing with frontal polymerization: (a) degree of cure; (b) elastic modulus; (c) norm of the Cauchy stress.

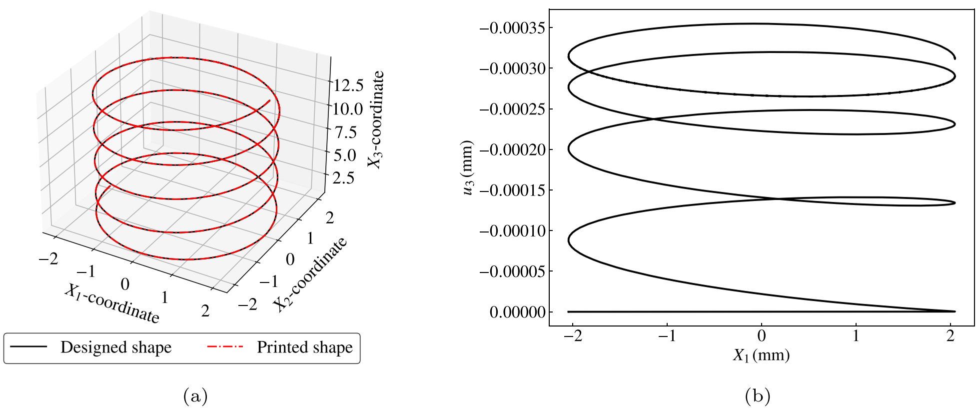

Fig. 13. Simulated printed coil structure: (a) comparison between designed and printed shape; (b) vertical deformation of the printed coil structure.

The numerical method is verified on a test case that has an analytical solution and good comparison is attained. The constitutive model for FP is validated via comparison with experimental data and with numerical simulations presented in the literature. Numerical test cases highlight the enhanced stability of the method that helps in the modeling of the rapidly evolving physical processes, as well as the propagation of steep reaction fronts that traverse through the domain across which the modulus of elasticity changes by orders of magnitude. The test case of FP in 3D block that is subjected to time periodic displacement boundary condition leads to large local strains that get trapped in the morphology of the material because of the curing induced formation of new bonds that lock the strains locally in the cured material. The model and method are also extended to frontal polymerization in extrusion-based additive manufacturing using direct ink writing (DIW). An algorithmic procedure for material extrusion is presented for printing the coil structure via DIW. These test cases highlight the mathematical and computational attributes of the proposed method for FP-based form free manufacturing. They also pave the way for the application of the model to open system thermodynamic frameworks where continuous influx of mass is accompanied with FP triggered concurrent evolution of material properties in DIW.

CRediT authorship contribution statement

Ignasius P.A. Wijaya: Writing – original draft, Visualization, Validation, Software, Methodology, Formal analysis. **Philippe Geubelle:** Writing – review & editing, Supervision, Methodology, Investigation, Data curation. **Arif Masud:** Writing – review & editing, Writing – original draft, Software, Methodology, Funding acquisition, Conceptualization.

Declaration of competing interest

The authors declare that they have no known competing financial interests or personal relationships that could have appeared to influence the work reported in this paper.

Acknowledgments

This work was partially supported by Sandia National Laboratory (SNL), United States Grant DOE-SNL-2318199.

Appendix. Derivation of the evolution Eq. (32) and the internal dissipation (33)

In this appendix, for clarity of presentation, we have opted to use the index notation. We first compute

$$\frac{\partial S_{kl}}{\partial E^i_{ij}} = -3\kappa(\gamma)\mathbb{J}_{ijkl} - 2\mu(\gamma)\mathbb{K}_{ijkl}. \tag{A.1}$$

where

$$\mathbb{J}_{ijkl} = \frac{1}{3}\delta_{ij}\delta_{kl}, \tag{A.2}$$

$$\mathbb{K}_{ijkl} = \left(\delta_{ik}\delta_{jl} - \frac{1}{3}\delta_{ij}\delta_{kl}\right). \tag{A.3}$$

Note that

$$\mathbb{J}_{ijkl}\mathbb{J}_{klmn} = \mathbb{J}_{ijmn}, \tag{A.4}$$

$$\mathbb{K}_{ijkl}\mathbb{K}_{klmn} = \mathbb{K}_{ijmn}, \tag{A.5}$$

$$\mathbb{J}_{ijkl}\mathbb{K}_{klmn} = \mathbb{K}_{ijkl}\mathbb{J}_{klmn} = 0, \tag{A.6}$$

$$\mathbb{K}_{ijkl} + \mathbb{J}_{ijkl} = \mathbb{I}_{ijkl} = \delta_{ik}\delta_{jl}. \tag{A.7}$$

Since (A.1) is written in spectral form, the inverse can be computed as follows.

$$\left[\frac{\partial \mathbf{S}}{\partial \mathbf{E}^i}\right]^{-1}_{pqkl} = -\frac{1}{3\kappa(\gamma)}\mathbb{J}_{pqkl} - \frac{1}{2\mu(\gamma)}\mathbb{K}_{pqkl}. \tag{A.8}$$

We can now compute

$$\left[\frac{\partial \mathbf{S}}{\partial \mathbf{E}^i}\right]^{-1}_{pqkl}\frac{\partial S_{kl}}{\partial \gamma} = -\frac{\kappa'(\gamma)}{3\kappa(\gamma)}E^e_{nn}\delta_{pq} - \frac{2\mu'(\gamma)}{2\mu(\gamma)}\left(E^e_{pq} - \frac{1}{3}E^e_{nn}\delta_{pq}\right). \tag{A.9}$$

Now, we can solve (31) as follows.

$$\begin{aligned}
0 &= -\frac{\partial S_{kl}}{2\partial E^i_{ij}}\dot{E}^i_{ij} - \frac{\partial S_{kl}}{2\partial \gamma}\dot{\gamma} \\
&\implies \left[\frac{\partial \mathbf{S}}{\partial \mathbf{E}^i}\right]^{-1}_{pqkl}\frac{\partial S_{kl}}{2\partial E^i_{ij}}\dot{E}^i_{ij} = -\left[\frac{\partial \mathbf{S}}{\partial \mathbf{E}^i}\right]^{-1}_{pqkl}\frac{\partial S_{kl}}{\partial \gamma}\dot{\gamma} \\
&\implies \dot{E}^i_{pq} = \frac{\dot{\kappa}(\gamma)}{3\kappa(\gamma)}E^e_{nn}\delta_{pq} + \frac{\dot{\mu}(\gamma)\dot{\gamma}}{\mu(\gamma)}\left(E^e_{pq} - \frac{1}{3}E^e_{nn}\delta_{pq}\right).
\end{aligned} \tag{A.10}$$

With the evolution Eq. (A.10), we compute the internal dissipation in Eq. (31). First, compute the first term.

$$\rho_0 \frac{\partial \Psi}{\partial E^i_{ij}} \dot{E}^i_{ij} = -\dot{\gamma} \left(\kappa'(\gamma)(E^e_{nn})^2 + 2\mu'(\gamma) \left((E^e_{ij})^2 - \frac{1}{3}(E^e_{nn})^2 \right) \right) = -2\rho_0 \frac{\partial \Psi}{\partial \gamma} \dot{\gamma}. \tag{A.11}$$

Using chain rule, the internal dissipation (22) can be written as follows.

$$\mathcal{D}_{int} = -\rho_0 \frac{\partial \Psi}{\partial E^i_{ij}} \dot{E}^i_{ij} - \rho_0 \frac{\partial \Psi}{\partial \gamma} \dot{\gamma} = 2\rho_0 \frac{\partial \Psi}{\partial \gamma} \dot{\gamma} - \rho_0 \frac{\partial \Psi}{\partial \gamma} \dot{\gamma} = \rho_0 \frac{\partial \Psi}{\partial \gamma} \dot{\gamma}. \tag{A.12}$$

For stiffening materials due to curing, $\dot{\gamma} \geq 0$, $\kappa' \geq 0$, and $\mu' \geq 0$. In this case, $\mathcal{D}_{int} \geq 0$.

Data availability

Data will be made available on request.

References

Anguiano, M., Gajendran, H., Hall, R.B., Rajagopal, K.R., Masud, A., 2020. Chemo-mechanical coupling and material evolution in finitely deforming solids with advancing fronts of reactive fluids. Acta Mech. 231 (5), 1933–1961.

Anguiano, M., Masud, A., 2021. Reduced mixture model and elastic response of chemically swollen solids: Application to Si oxidation and lithiation. Appl. Eng. Sci. 6, 100039.

Anguiano, M., Masud, A., Rajagopal, K.R., 2022. Mixture model for thermo–chemo–mechanical processes in fluid-infused solids. Internat. J. Engrg. Sci. 174, 103576.

Armero, F., Simo, J.C., 1992. A new unconditionally stable fractional step method for non-linear coupled thermomechanical problems. Internat. J. Numer. Methods Engrg. 35 (4), 737–766.

Aw, J.E., 2019. Simultaneous Three-Dimensional Printing and Frontal Polymerization of Dicyclopentadiene Resin (Ph.D. thesis). University of Illinois Urbana-Champaign.

Aw, J.E., Zhang, X., Nelson, A.Z., Dean, L.M., Yourdkhani, M., Ewoldt, R.H., Geubelle, P.H., Sottos, N.R., 2022. Self-regulative direct ink writing of frontally polymerizing thermoset polymers. Adv. Mater. Technol. 7 (9), 2200230.

Ayub, M., Masud, A., 2003. A new stabilized formulation for convective-diffusive heat transfer. Numer. Heat Transfer B 44 (1), 1–23.

Bažant, Z.P., 1979. Thermodynamics of solidifying or melting viscoelastic material. J. Eng. Mech. Div. 105 (6), 933–952.

Bažant, Z.P., L'Hermite, R., International Union of Testing and Research Laboratories for Materials and Structures, (U.S.), N.S.F., 1988. Mathematical Modeling of Creep and Shrinkage of Concrete. In: Wiley Series in Numerical Methods in Engineering, Wiley, Chichester, New York.

Brezzi, F., Fortin, M., 1991. Mixed and Hybrid Finite Element Methods. In: Springer Series in Computational Mathematics, vol. 15, Springer, New York Berlin Heidelberg.

Bulíček, M., Málek, J., Pr̊uša, V., 2019. Thermodynamics and stability of non-equilibrium steady states in open systems. Entropy 21 (7), 704.

Chechilo, N., Khvilivitskii, R., Enikolopyan, N., 1972. Propagation of the polymerization reaction. In: Dokl. Akad. Nauk SSSR, vol. 204, pp. 1180–1181.

Chester, S.A., Anand, L., 2011. A thermo-mechanically coupled theory for fluid permeation in elastomeric materials: Application to thermally responsive gels. J. Mech. Phys. Solids 59 (10), 1978–2006.

Chester, S.A., Di Leo, C.V., Anand, L., 2015. A finite element implementation of a coupled diffusion-deformation theory for elastomeric gels. Int. J. Solids Struct. 52, 1–18.

Chipman, F.H., 1971. A-stable Runge–Kutta processes. BIT 11 (4), 384–388.

Coleman, B.D., Gurtin, M.E., 1967. Thermodynamics with internal state variables. J. Chem. Phys. 47 (2), 597–613.

Coleman, B.D., Noll, W., 1963. The thermodynamics of elastic materials with heat conduction and viscosity. Arch. Ration. Mech. Anal. 13 (1), 167–178.

Ehle, B.L., 1969. On Padé Approximations to the Exponential Function and A-Stable Methods for the Numerical Solution of Initial Value Problem (Ph.D. thesis). University of Waterloo.

Frulloni, E., Salinas, M.M., Torre, L., Mariani, A., Kenny, J.M., 2005. Numerical modeling and experimental study of the frontal polymerization of the diglycidyl ether of bisphenol A/diethylenetriamine epoxy system. J. Appl. Polym. Sci. 96 (5), 1756–1766.

Gajendran, H., Hall, R.B., Masud, A., Rajagopal, K.R., 2018. Chemo-mechanical coupling in curing and material-interphase evolution in multi-constituent materials. Acta Mech. 229 (8), 3393–3414.

Goli, E., Peterson, S., Geubelle, P., 2020. Instabilities driven by frontal polymerization in thermosetting polymers and composites. Compos. Part B: Eng. 199, 108306.

Goli, E., Robertson, I.D., Geubelle, P.H., Moore, J.S., 2018. Frontal polymerization of dicyclopentadiene: A numerical study. J. Phys. Chem. B 122 (16), 4583–4591.

Hughes, T.J., 1995. Multiscale phenomena: Green's functions, the Dirichlet-to-Neumann formulation, subgrid scale models, bubbles and the origins of stabilized methods. Comput. Methods Appl. Mech. Engrg. 127 (1–4), 387–401.

Ivanoff, D.G., Sung, J., Butikofer, S.M., Moore, J.S., Sottos, N.R., 2020. Cross-linking agents for enhanced performance of thermosets prepared via frontal ring-opening metathesis polymerization. Macromolecules 53 (19), 8360–8366.

Kannan, K., Rajagopal, K.R., 2011. A thermodynamical framework for chemically reacting systems. Z. Angew. Math. Phys. 62 (2), 331–363.

Kumar, A., Dean, L.M., Yourdkhani, M., Guo, A., BenVau, C., Sottos, N.R., Geubelle, P.H., 2022. Surface pattern formation induced by oscillatory loading of frontally polymerized gels. J. Mech. Phys. Solids 168, 105055.

Kumar, A., Gao, Y., Geubelle, P.H., 2021. Analytical estimates of front velocity in the frontal polymerization of thermoset polymers and composites. J. Polym. Sci. 59 (11), 1109–1118.

Kumar, A., Zakoworotny, M., Bonner, F.J.B., Aw, J.E., Sottos, N.R., Tawfick, S.H., Geubelle, P.H., 2024. A thermo–chemo–mechanical model for material extrusion of frontally polymerizing thermoset polymers. Addit. Manuf. 80, 103972.

Lawson, J.D., 1966. An order five Runge–Kutta process with extended region of stability. SIAM J. Numer. Anal. 3 (4), 593–597.

Liu, Q., Abueidda, D., Vyas, S., Gao, Y., Koric, S., Geubelle, P.H., 2024. Adaptive data-driven deep-learning surrogate model for frontal polymerization in dicyclopentadiene. J. Phys. Chem. B 128 (5), 1220–1230.

Lloyd, E.M., Feinberg, E.C., Gao, Y., Peterson, S.R., Soman, B., Hemmer, J., Dean, L.M., Wu, Q., Geubelle, P.H., Sottos, N.R., Moore, J.S., 2021. Spontaneous patterning during frontal polymerization. ACS Central Sci. 7 (4), 603–612.

Loeffel, K., Anand, L., 2011. A chemo-thermo-mechanically coupled theory for elastic–viscoplastic deformation, diffusion, and volumetric swelling due to a chemical reaction. Int. J. Plast. 27 (9), 1409–1431.

Mariani, A., Malucelli, G., 2023. Polymer hydrogels and frontal polymerization: A winning coupling. Polymers 15 (21), 4242.

Masud, A., 2004. Stabilized methods in solid mechanics. In: Finite Element Methods: 1970's and Beyond. pp. 172–187.

Masud, A., Anguiano, M., Harari, I., 2020. Modeling of steep layers in singularly perturbed diffusion–reaction equation via flexible fine-scale basis. Comput. Methods Appl. Mech. Engrg. 372, 113343.

Masud, A., Chen, P., 2019. Thermoelasticity at finite strains with weak and strong discontinuities. Comput. Methods Appl. Mech. Engrg. 347, 1050–1084.

Masud, A., Franca, L.P., 2008. A hierarchical multiscale framework for problems with multiscale source terms. Comput. Methods Appl. Mech. Engrg. 197 (33–40), 2692–2700.

Masud, A., Kwack, J., 2008. A stabilized mixed finite element method for the first-order form of advection–diffusion equation. Internat. J. Numer. Methods Fluids 57 (9), 1321–1348.

Masud, A., Truster, T.J., 2013. A framework for residual-based stabilization of incompressible finite elasticity: Stabilized formulations and F-bar methods for linear triangles and tetrahedra. Comput. Methods Appl. Mech. Engrg. 267, 359–399.

Masud, A., Xia, K., 2006. A variational multiscale method for inelasticity: Application to superelasticity in shape memory alloys. Comput. Methods Appl. Mech. Engrg. 195 (33–36), 4512–4531.

Nedjar, B., 2021. On a geometrically nonlinear incremental formulation for the modeling of 3D concrete printing. Mech. Res. Commun. 116, 103748.

Nedjar, B., 2022. Incremental viscoelasticity at finite strains for the modelling of 3D concrete printing. Comput. Mech. 69 (1), 233–243.

Paul, J.E., Gao, Y., Go, Y.K., Rodriguez Koett, L.E., Sharma, A., Chen, M., Lessard, J.J., Topkaya, T., Leal, C., Moore, J.S., Geubelle, P.H., Sottos, N.R., 2024. Controlled patterning of crystalline domains by frontal polymerization. Nature 634 (8032), 85–90.

Pojman, J., 2012. Frontal polymerization. In: Polymer Science: A Comprehensive Reference. Elsevier, pp. 957–980.

Robertson, I.D., Yourdkhani, M., Centellas, P.J., Aw, J.E., Ivanoff, D.G., Goli, E., Lloyd, E.M., Dean, L.M., Sottos, N.R., Geubelle, P.H., Moore, J.S., White, S.R., 2018. Rapid energy-efficient manufacturing of polymers and composites via frontal polymerization. Nature 557 (7704), 223–227.

Simo, J.C., Hughes, T.J.R., 1998. Computational inelasticity. In: Interdisciplinary Applied Mathematics Mechanics and Materials, vol. 7, Springer, New York Heidelberg Berlin.

Simo, J., Miehe, C., 1992. Associative coupled thermoplasticity at finite strains: Formulation, numerical analysis and implementation. Comput. Methods Appl. Mech. Engrg. 98 (1), 41–104.

Solovyov, S.E., Ilyashenko, V.M., Pojman, J.A., 1997. Numerical modeling of self-propagating polymerization fronts: The role of kinetics on front stability. Chaos: Interdiscip. J. Nonlinear Sci. 7 (2), 331–340.

Steinebach, G., 2020. Improvement of Rosenbrock–Wanner method RODASP: Enhanced coefficient set and MATLAB implementation. In: Reis, T., Grundel, S., Schöps, S. (Eds.), Progress in Differential-Algebraic Equations II. Springer International Publishing, Cham, pp. 165–184.

Suslick, B.A., Hemmer, J., Groce, B.R., Stawiasz, K.J., Geubelle, P.H., Malucelli, G., Mariani, A., Moore, J.S., Pojman, J.A., Sottos, N.R., 2023. Frontal polymerizations: From chemical perspectives to macroscopic properties and applications. Chem. Rev. 123 (6), 3237–3298.

Truesdell, C., 1984. Rational Thermodynamics. Springer New York, New York, NY.

Truesdell, C., Noll, W., 2004. The Non-Linear Field Theories of Mechanics. Springer Berlin Heidelberg, Berlin, Heidelberg.

Truster, T.J., Chen, P., Masud, A., 2015. Finite strain primal interface formulation with consistently evolving stabilization. Internat. J. Numer. Methods Engrg. 102 (3–4), 278–315.

Vyas, S., Parikh, N., Price, T., Patel, D., Le, T., Geubelle, P., Sottos, N., 2024. Through-thickness frontal polymerization: Process development and optimization. Compos. Part A: Appl. Sci. Manuf. 180, 108084.

Wcisło, B., Pamin, J., Rose, L., Menzel, A., 2023. On spatial vs referential isotropic Fourier's law in finite deformation thermomechanics. Eng. Trans. 71 (1), 111–140.

Wijaya, I.P.A., Kreiger, E., Masud, A., 2022. An elastic–inelastic model and embedded bounce-back control for layered printing with cementitious materials. Internat. J. Numer. Methods Engrg. 123 (21), 5098–5125.

Wijaya, I.P.A., Kreiger, E.L., Masud, A., 2024. Modeling of concrete printing process with frictional interface. ACI Struct. J. 121 (2), 71–85.

Zakoworotny, M., Balta Bonner, F.J., Kumar, A., Aw, J.E., Tawfick, S.H., Ewoldt, R.H., Sottos, N.R., Geubelle, P.H., 2024. Rheological modeling of frontal-polymerization-based direct ink writing of thermoset polymers. Comput. Methods Appl. Mech. Engrg. 418, 116565.